

ENHANCED PIEZOELECTRIC RESPONSE OF ELECTROSPUN PVDF WITH
ZNO NANORODS: THE COMPARISON OF THREE ZNO ADDITION METHODS

A Dissertation

Presented to the Faculty of the Graduate School

of Cornell University

In Partial Fulfillment of the Requirements for the Degree of

Doctor of Philosophy

by

Minji Kim

May 2019

© 2019 Minji Kim

ENHANCED PIEZOELECTRIC RESPONSE OF ELECTROSPUN PVDF WITH ZNO NANORODS: THE COMPARISON OF THREE ZNO ADDITION METHODS

Minji Kim, Ph.D.

Cornell University 2019

A novel breathable piezoelectric membrane was developed by adding zinc oxide (ZnO) to electrospun polyvinylidene fluoride (PVDF) nanofibers. Notable improvements in the piezoelectric response of PVDF membrane was achieved without compromising the breathability, conformability, or safety of the material.

Three ZnO nanorod addition methods were investigated: fillers in electrospinning solution, hydrothermal growth on the fiber surface, and electrospraying on the PVDF membrane surface. Due to its high piezoelectric coefficient values, PVDF is one of the most frequently used piezoelectric polymers. However, its piezoelectric response requires further improvements to use PVDF as high-performance sensors or energy harvesters. Previous studies have identified piezoelectric ceramic and polymer composites with a remarkably improved piezoelectric constant. However, such composites often lack breathability, and some contain piezoelectric ceramics with heavy metals, thus limiting their use in wearable applications. The said limitations can be alleviated by electrospinning piezoelectric polymers into porous membranes and by selecting non-toxic piezoelectric ceramics. Unlike many piezoelectric ceramics containing heavy metals, ZnO is a non-toxic material that has been widely used in many fields and applications, including cosmetics. The fabrication process is simple and

economical since it requires no additional poling for PVDF membranes after electrospinning them in a high electric field.

The poling direction of PVDF was studied by placing the membrane in a high electric field and observing the membrane's movements. The electrospun PVDF have dipole alignment both in the fiber-axis direction and membrane thickness direction, as well as a stronger alignment in the fiber-axis direction.

A breathable and flexible conductive textile material was explored and compared to an aluminum foil. The conductive material's mechanical properties, such as breathability and flexibility, indicated that it is a wearable material. Also, its performance as an electrode material was compared to that of aluminum foils and sheets, and the material seems suitable for electrodes.

BIOGRAPHICAL SKETCH

Minji Kim was born in Seoul, the Republic of Korea. She studied at the Department of Clothing and Textiles at Yonsei University (Seoul, Korea) from 2007 and developed a passion for innovative textile materials. She decided to continue studying at graduate school to explore the field of polymer and fiber science. After graduating with her BS degree in the fall of 2011, she started her graduate studies in fiber science at the Department of Fiber Science and Apparel Design at Cornell University (Ithaca, NY, USA) in the fall of 2012. In 2014, she earned her MS degree and continued her doctorate in fiber science at Cornell University.

To my mother

ACKNOWLEDGMENTS

The journey to a doctorate can be lonely and strenuous. It would not have been possible to get this far without the support of numerous people.

First, I would like to thank my advisor Dr. Jintu Fan for his continuous support from the beginning of my graduate studies until the end. Dr. Fan worked with me on everything, including ways to approach research problems, how to design and execute experiments, and how to think and ask questions while completing a Ph.D. dissertation. He provided me room to grow and become an independent researcher, showed me how to be persistent to accomplish my goals, and taught me not to give up. Without his guidance, I could not have finished this dissertation.

I would also like to express my deepest gratitude to my special committee. Dr. Edwin C. Kan was always been there to advise me on piezoelectric materials and electrical engineering, proofread and mark up my papers, and foster my career development. I am also indebted to Dr. Yong L. Joo for offering his time and expertise whenever I faced challenges.

I would also like to thank my field member, Dr. Margaret W. Frey, and the director of graduate studies, Dr. Anil Netravali, for their support and encouragement in my research, teaching assistantships, and career development.

Part of this work was supported by the Student Research Support Grant Program of the American Association of Textile Chemists and Colorists (AATCC) Foundation, and the Herbert and Lillian Powell, Mary Purchase, and Evelyn E. Stout Graduate Fellowship from the College of Human Ecology, Cornell University.

Last, but certainly not least, I would like to thank my father, Dr. Il Kon Kim, for his endless support and love, as well as my brother, Jongoh Kim, for his constant caring and encouragement.

TABLE OF CONTENTS

BIOGRAPHICAL SKETCH.....	v
ACKNOWLEDGMENTS.....	vii
TABLE OF CONTENTS.....	ix
LIST OF FIGURES.....	xiii
LIST OF TABLES.....	xviii
CHAPTER 1. THE MOTIVATION FOR THE WORK.....	1
CHAPTER 2. ZNO NANORODS AS FILLERS OF PVDF NANOFIBERS	3
2.1. Introduction	3
2.2. Materials and Methods	3
2.2.1. Hydrothermal Synthesis of ZnO Nanorods	3
2.2.2. Electrospinning of PVDF Nanofiber Mats with ZnO Nanorod Fillers	3
2.2.3. Characterization.....	4
2.2.4. Piezoelectric Testing	5
2.3. Results and Discussion	6
2.3.1. Material Analysis.....	6
2.3.2. Piezoelectric Measurements	10
2.4. Conclusions	13
CHAPTER 3. THE GROWTH OF ZNO NANORODS ON PVDF NANOFIBER SURFACES.....	14
3.1. Introduction	14
3.2. Materials and Methods	14
3.2.1. Electrospinning of PVDF Nanofiber Mats.....	14
3.2.2. Hydrothermal Growth of ZnO Nanorods	15
3.2.3. Characterization.....	16

3.2.4. Piezoelectric Testing	17
3.3. Results and Discussion	18
3.3.1. Material Analysis.....	19
3.3.2. Piezoelectric Measurements	26
3.4. Conclusions	27
CHAPTER 4. ELECTROSPRAYING OF ZNO NANORODS ON THE SURFACE OF PVDF NANOFIBER MATS	28
4.1. Introduction	28
4.2. Materials and Methods	28
4.2.1. Electrospinning of PVDF Nanofiber Mats	28
4.2.2. Hydrothermal Synthesis of ZnO Nanorods	29
4.2.3. Electrospaying of ZnO Nanorods onto PVDF Nanofiber Mats	29
4.2.4. Characterization.....	29
4.2.5. Piezoelectric Testing	30
4.3. Results and Discussion	31
4.3.1. Material Analysis.....	31
4.3.2. Piezoelectric Measurement.....	36
4.4. Conclusions	38
CHAPTER 5. THE COMPARISON OF THREE TYPES OF PVDF AND ZNO NANOFIBROUS COMPOSITES.....	39
5.1. Introduction	39
5.2. Materials and Methods	39
5.2.1. Electrospinning of PVDF Nanofiber Mats	39
5.2.2. Hydrothermal Synthesis of ZnO Nanorods	40
5.2.3. Electrospaying of ZnO Nanorods onto PVDF Nanofiber Mat.....	40
5.2.4. Hydrothermal Growth of ZnO Nanorods	40
5.2.5. Characterization.....	42
5.2.6. Piezoelectric Testing	43

5.3. Results and Discussion	44
5.3.1. Material Analysis.....	44
5.3.2. Piezoelectric Measurements	52
5.3.3. Polarization Direction.....	54
5.4. Conclusions	60
CHAPTER 6. BREATHABLE NANOGENERATORS	62
6.1. Introduction	62
6.2. Materials and Methods	62
6.2.1. Electrode Materials.....	62
6.2.2. Breathability	62
6.2.3. Piezoelectric Testing	63
6.3. Results and Discussion	63
6.3.1. Mechanical Properties	63
6.3.2. Piezoelectric Measurement Comparison of Aluminum Foil and Conductive-Knit Fabric as Electrodes.....	65
6.4. Conclusions	67
CHAPTER 7. COMPARISON OF CONDUCTIVE KNITS AND METAL SHEETS AS ELECTRODES	68
7.1. Introduction	68
7.2. Materials and Methods	68
7.2.1. Electrode Materials.....	68
7.2.2. Piezoelectric Testing	68
7.3. Results and Discussion	69
7.3.1. Open-circuit Voltage	69
7.3.2. Current with a Resistive Load	71
7.4. Conclusions	73
CHAPTER 8. CONCLUSIONS AND FUTURE WORKS.....	74

8.1. Conclusions	74
8.2. Recommendations for Future Research.....	75
REFERENCES	77

LIST OF FIGURES

Figure 1. (a) A TEM image of the ZnO nanorod fillers in PVDF nanofibers; (b) an FESEM image of the ZnO nanorod fillers in PVDF nanofibers; (c) an enlarged image; and (d) a histogram of the diameter distribution of electrospun PVDF nanofibers.	7
Figure 2. FTIR spectra showing the effect of the addition of ZnO nanorod fillers to PVDF crystalline phases.	8
Figure 3. TGA of the PVDF membrane and ZnO+PVDF.	9
Figure 4. XRD spectra of the PVDF membrane and ZnO+PVDF.	10
Figure 5. The schematic illustration of the breathable fibrous nanogenerator.	11
Figure 6. Nanogenerator characteristics of PVDF and ZnO+PVDF 15 cm ² fiber mats: (a) load curves with resistive loads of 0.47, 15, 30, and 60 MΩ; and (b) transient closed-circuit current measurements with a 15 MΩ resistive load.	12
Figure 7. (a) An FESEM image of the smaller type ZnO nanorods grown on the surface of the electrospun PVDF nanofiber; (b) a histogram of the length and diameter distributions of the smaller ZnO nanorods; (c) an image of the electrospun PVDF nanofiber; and (d) a histogram of the diameter distribution of electrospun PVDF nanofibers.	20
Figure 8. FTIR spectra showing the effect of (a) electrospinning and (b) hydrothermal growth of ZnO nanorods on PVDF crystalline phases.	23

Figure 9. XRD spectra of the (a) PVDF pellet and PVDF nanofibers; and (b) the electrospun PVDF nanofibers before and after the hydrothermal growth of ZnO nanorods.....	25
Figure 10. TGA of the PVDF membrane and ZnO@PVDF.	25
Figure 11. Nanogenerator characteristics of PVDF and ZnO@PVDF 15 cm ² fiber mats: (a) load curves with resistive loads of 0.47, 15, 30, and 60 MΩ; and (b) transient closed-circuit current measurements with a 15 MΩ resistive load.....	27
Figure 12. (a) An FESEM image of the ZnO nanorods electrospayed on the surface of the electrospun PVDF nanofiber (ZnO/PVDF); and (b) a histogram of the length and diameter distributions of ZnO nanorods.....	32
Figure 13. FTIR spectra showing the effect of electrospaying of ZnO nanorods on PVDF crystalline phases.	33
Figure 14. TGA of the PVDF membrane and ZnO/PVDF.....	34
Figure 15. XRD spectra of the PVDF membrane and ZnO/PVDF.	35
Figure 16. Nanogenerator characteristics of PVDF and ZnO/PVDF 15 cm ² fiber mats: (a) load curves with resistive loads of 0.47, 15, 30, and 60 MΩ; and (b) transient closed-circuit current measurements with a 15 MΩ resistive load.	37
Figure 17. FESEM images of the (a) electrospun PVDF nanofibers; (c) ZnO nanorod fillers in PVDF nanofibers (ZnO+PVDF); (e) ZnO growth on a PVDF nanofiber surface (ZnO@PVDF); (g) ZnO nanorods electrospayed onto PVDF nanofiber mats (ZnO/PVDF). Nanofiber diameter analysis of	

electrospun (b) PVDF and (d) PVDF with ZnO fillers. Diameter and length analysis of (f) ZnO nanorods grown at 60°C; (h) ZnO nanorods synthesized at 150°C; (i) diameter comparison; and (j) length comparison of ZnO grown at 60°C and 150°C.	46
Figure 18. FTIR spectra showing the effect of the three ZnO nanorod addition methods to PVDF crystalline phases.	48
Figure 19. Peaks of FTIR spectra corresponding to α and β crystalline phases of PVDF: (a) α , 614 cm^{-1} ; (b) α , 762 cm^{-1} ; (c) α , 796 cm^{-1} ; (d) β , 840 cm^{-1} ; (e) α , 975 cm^{-1} ; and (f) β , 1276 cm^{-1}	49
Figure 20. TGA of the PVDF membrane, ZnO+PVDF, ZnO@PVDF, and ZnO/PVDF.....	50
Figure 21. XRD spectra of the PVDF membrane and three types of ZnO and PVDF composites.....	52
Figure 22. Nanogenerator characteristics of 15 cm^2 fiber mats: (a) load curves with resistive loads of 0.47, 15, 30, and 60 $\text{M}\Omega$; and (b) transient closed-circuit current measurements with a 15 $\text{M}\Omega$ resistive load.....	53
Figure 23. Polarization direction compression study in thickness direction: (a) the average open-circuit voltage response of one-layer PVDF and two layers stacked in the opposite thickness direction; and (b) transient open-circuit voltage measurements.....	56
Figure 24. Electrospun PVDF membrane cut direction: (a) the rotation direction of the collecting drum (Lr); and (b) perpendicular to the drum-rotation direction (Lp).....	57

Figure 25. Testing setup for PVDF membrane behavior in the high electric field. 58

Figure 26. Green arrows indicate that the membrane thickness is facing the observer, as well as the direction of the thickness-polarization direction. Solid red arrows indicate the top surface-facing observer and the drum-rotation direction. Red arrows in dashes indicate the bottom-facing observer and the drum-rotation direction. (a) PVDF membrane rectangle length aligned to the drum-collector rotation direction and the membrane thickness-facing observer (*Lrt*); (b) Membrane rectangle length perpendicular to the collector rotation direction and the top surface-facing observer (*Lrf-t*); (c) Membrane rectangle length aligned to the collector rotation direction and the bottom surface-facing front (*Lrf-b*); (d) PVDF mat rectangle length perpendicular to the drum-collector rotation direction and the membrane thickness-facing observer (*Lpt*); (e) Membrane rectangle length perpendicular to the collector rotation direction and the top surface-facing front (*Lpf-t*); (f) Membrane rectangle length perpendicular to the collector rotation direction and the bottom surface-facing front (*Lpf-b*). 59

Figure 27. (a) The breathable fibrous nanogenerator with conductive knits and (b) the non-breathable nanogenerator with aluminum foil..... 63

Figure 28. Open-circuit voltage measurements under a 0.10 MPa impact of 1 Hz frequency: (a) a conductive-knit electrode nanogenerator and an (b) aluminum-foil electrode nanogenerator. The black lines in dashes represent PVDF, while the red lines stand for ZnO@PVDF..... 66

Figure 29. (a) The flexible fibrous nanogenerator with conductive-knit electrodes and
(b) the solid nanogenerator with aluminum-sheet electrodes. 69

Figure 30. Transient open-circuit voltage measurements under 0.10 MPa impacts of 1
Hz frequency: (a) the effect of aluminum sheets' weight-restricting
membrane thickness on recovery from compression over a long period of
time and (b) enlarged responses over a short time. The black lines represent
conductive-knit electrodes, and purple lines denote aluminum-sheet
electrodes. 70

Figure 31. The transient closed-circuit current of the conductive-knit (black dash) and
aluminum-sheet (purple line) electrodes with a 470 k Ω resistive load under
a 0.10 MPa impact of 1 Hz frequency. 72

LIST OF TABLES

Table 1. Measured closed-circuit current and voltage averages with conductive-knit electrodes.....	12
Table 2. Measured closed-circuit current and voltage averages with conductive-knit electrodes.....	27
Table 3. Measured closed-circuit current and voltage averages with conductive-knit electrodes.....	37
Table 4. Comparison of closed-circuit current and voltages of electrospun PVDF and three different types of ZnO and PVDF nanofiber composites.....	54
Table 5. Performance comparison of ZnO+PVDF, ZnO@PVDF, and ZnO/PVDF with conductive-knit electrodes to other works of flexible and breathable films.	61
Table 6. Water-vapor permeability (WVP) for various membranes and fabrics.....	65
Table 7. Open-circuit voltages for piezoelectric samples under a 0.10 MPa impact of 1 Hz frequency.	66
Table 8. Open-circuit voltages (V_{oc}) and a closed-circuit current with a 470 k Ω resistive load (V_{cc}) comparison for conductive-knit and aluminum-sheet electrodes under a 0.10 MPa impact of 1 Hz frequency.....	72

CHAPTER 1. THE MOTIVATION FOR THE WORK

Interest in wearable piezoelectric materials has grown tremendously due to the increasing need for powering mobile devices, achieving sustainable operations, and measuring long-term biometric data.¹⁻³ Piezoelectric polymers are attractive for wearables due to their flexibility and conformability compared to piezoelectric ceramic materials.⁴⁻⁷ Poly(vinylidene fluoride) (PVDF) and its copolymers are known to have very large and stable ferroelectric, piezoelectric, and pyroelectric properties among polymers. Also, it has high resistivity to daily chemicals, which makes it safe to use against cleaning agents, skin products, and sweat.⁸ However, PVDF and its copolymers still have significantly lower piezoelectric coefficients than piezoelectric ceramics,⁹⁻¹² and further improvement is desirable for sensor and energy-harvester applications. Many researchers have demonstrated that incorporating piezoelectric ceramics into PVDF to create a composite material can achieve a higher piezoelectric constant and an excellent electromechanical coupling factor.¹³⁻¹⁹

The chemical resistivity of PVDF also provides stability and safety for use next to human skin. When selecting piezoelectric ceramics to be embedded in a PVDF matrix, the potential health hazard is one of the most important factors to be considered.^{20,21} Lead zirconate titanate (PZT) is one of the most common piezoelectric ceramics due to its high piezoelectric response. However, PZT poses risks since it contains highly toxic lead. Lead-free piezoelectric materials have been extensively researched to replace PZT,²²⁻²⁵ and zinc oxide (ZnO) shows strong potential for next-to-skin applications. Sunscreen manufacturers commonly use ZnO in their products, and the FDA has approved its application.²⁶⁻²⁹ Also, among lead-free piezoelectric ceramics, ZnO has one of the lowest hydrothermal reaction temperatures.³⁰⁻³³ The low reaction temperature

was preferred for this research, as it allows the avoidance of an additional poling step after the addition of ceramics to the polymer matrix. In previous researches, ZnO was added to a non-porous polymer matrix as thin films to fabricate more flexible nanogenerators to overcome the brittleness and limited yield strength of inorganic materials.³⁴⁻³⁷ These nanogenerators have a reasonable piezoelectric performance, but the films are not breathable, which limits their use in wearable applications.

Piezoelectric polymers can be made into thin films or fibers. Fibrous materials are both breathable and flexible; therefore, they are more suitable for wearable applications than for thin films. Also, one-dimensional PVDF fibers can have higher piezoelectric energy-conversion efficiency than films.^{38,39} However, so far, piezoelectric fibrous materials have been assembled with at least two layers of non-breathable materials.¹⁵⁻¹⁸ For example, solid metal films have been used as electrodes, as well as plastics as an external casing to protect from ambient contamination and to ensure good electrical contact. These material additions compromise the flexibility and breathability of the fibrous material required for wearable applications.

For this study, three types of ZnO and PVDF composite nanofibrous material were compared to observe the piezoelectric response. The goal was to find the addition method resulting in the greatest improvement in piezoelectricity. First, ZnO nanorods were added as fillers in a PVDF spinning solution, grown on the surface of PVDF fibers, and, finally, electrosprayed onto the electrospun PVDF fiber mat.

Breathable and flexible fibrous nanogenerators with conductive textile electrodes without impermeable casing were explored by testing the breathability of the electrode and piezoelectric materials.

CHAPTER 2. ZNO NANORODS AS FILLERS OF PVDF NANOFIBERS

2.1. Introduction

Using ceramics as fillers in a polymer matrix is one of the most common ceramic/polymer composite fabrication methods. The filler addition method was explored first.

2.2. Materials and Methods

2.2.1. Hydrothermal Synthesis of ZnO Nanorods

Single-crystalline ZnO nanorods with small diameters were prepared by a hydrothermal synthesis method in an autoclave. For this study, 20 mL of 0.1 M of zinc acetate dihydrate ($\text{Zn}(\text{Ac})_2 \cdot 2\text{H}_2\text{O}$) solution in ethanol and 40 mL of 0.5 M sodium hydroxide (NaOH) in ethanol was transferred to a Teflon-lined stainless steel autoclave and heated at 150°C for 15 h.⁴⁰ The solution with white precipitate was vacuum filtered with 0.4 μm membranes.

2.2.2. Electrospinning of PVDF Nanofiber Mats with ZnO Nanorod Fillers

In this research, PVDF with a ZnO filler solution of 20 wt% of PVDF was used, and the ZnO filler amount was 5 wt% of PVDF. First, ZnO nanorods were added to the DMF–acetone solvent mixture (7/3 v/v) and then sonicated for 90 min. After sonication, PVDF pellets were added and stirred with a magnetic stirring bar at 70°C for 5 h.

2.2.3. *Characterization*

Field-emission scanning electron microscope (FESEM) images were taken using a Gemini 500 model (ZEISS, Oberkochen, Germany) with an accelerating voltage of 1 keV. To extract the detailed geometry with better focus and to reduce the charging effect under an FESEM, the samples were partially sputter coated with palladium/gold. The average PVDF fiber diameter, as well as the ZnO nanorod length and diameter, was determined by FESEM images over 30 fibers with the ImageJ software (NIH, Bethesda, Rockville, MD, USA).⁴¹

Transmission electron microscope (TEM) images were taken using a T12 Spirit model (FEI, Lausanne, Switzerland) with an accelerating voltage of 120 keV. Nanofiber samples were placed between a copper oyster grid.

The crystallography of PVDF nanofibers and ZnO nanorods was examined by X-ray diffraction (XRD) with the powder diffractometer (D8 GADDS, Bruker), and Cu-K α radiation (= 1.54 Å) at a 0.02° scanning step and an operating voltage of 40 kV and a current of 40 mA were used.

Fourier-transform infrared (FTIR) spectroscopy from 4,000 to 650 cm⁻¹ (Frontier FTIR, PerkinElmer, Waltham, MA, USA) was performed at room temperature to evaluate the polymer crystalline phase. In addition, FTIR spectra were collected with 16 scans and a resolution of 4 cm⁻¹.

Thermal gravimetric analyses (TGA) were used to determine the amount of ZnO added to PVDF nanofibers (Q500 Thermogravimetric Analyzer, TA Instruments, New Castle, DE, USA) by heat removal of PVDF. Samples were heated up from room

temperature to 990°C with the rate of 10°C/min on a ceramic pan under a nitrogen ambient.

2.2.4. Piezoelectric Testing

The piezoelectric testing module was assembled by sandwiching the piezoelectric nanofiber mat between two electrodes made by conductive fabric (cotton and silver blend double jersey knit purchased from LessEMF, Latham, NY, USA). Wires were connected to the electrodes using conductive ink and epoxy.

The piezoelectric performance of the electrospun samples was evaluated by periodic tensile testing in a customized setup with a motorized actuator controlled by a controller and a module (ni-cRIO 9036 and ni-9503, National Instruments, Austin, TX, USA), a pressure sensor (LC201-300/N, Newport Electronics, Santa Ana, CA, USA), an electrometer (6517B, Keithley Instruments, Cleveland, OH, USA), a multimeter (34470A, Keysight, Santa Rosa, CA, USA), a source meter (2400, Keithley, Cleveland, OH, USA), and a programmable DC power supply (9130, BK Precision, Yorba Linda, CA, USA). The open-circuit voltage and the closed-circuit current were measured with a Keithley 6517B electrometer and a Keithley 2400 source meter, respectively. The testing head movement was set to 1 Hz, and the impact pressure was set to 0.10 MPa, which is within the human foot pressure range of 0–0.20 MPa,^{42–44} although the applications are not limited to shoes. LabView software (National Instruments, Austin, TX, USA) was used to control all the components and to record voltage and current outputs synchronously.

2.3. Results and Discussion

The effects of adding ZnO nanorods as fillers of PVDF nanofibers (e.g., morphology, PVDF β phase, crystallinity, and piezoelectricity) were investigated.

2.3.1. Material Analysis

The morphology of PVDF nanofibers with ZnO nanorods as fillers was examined using TEM and FESEM images. Figure 1 displays the morphology, the size distribution of the PVDF nanofiber diameter, the ZnO nanorod diameter, and the ZnO nanorod length. In this study, the ZnO nanorods had an average diameter of 31 ± 22 nm and a length of 228 ± 613 nm (Figure 1d).

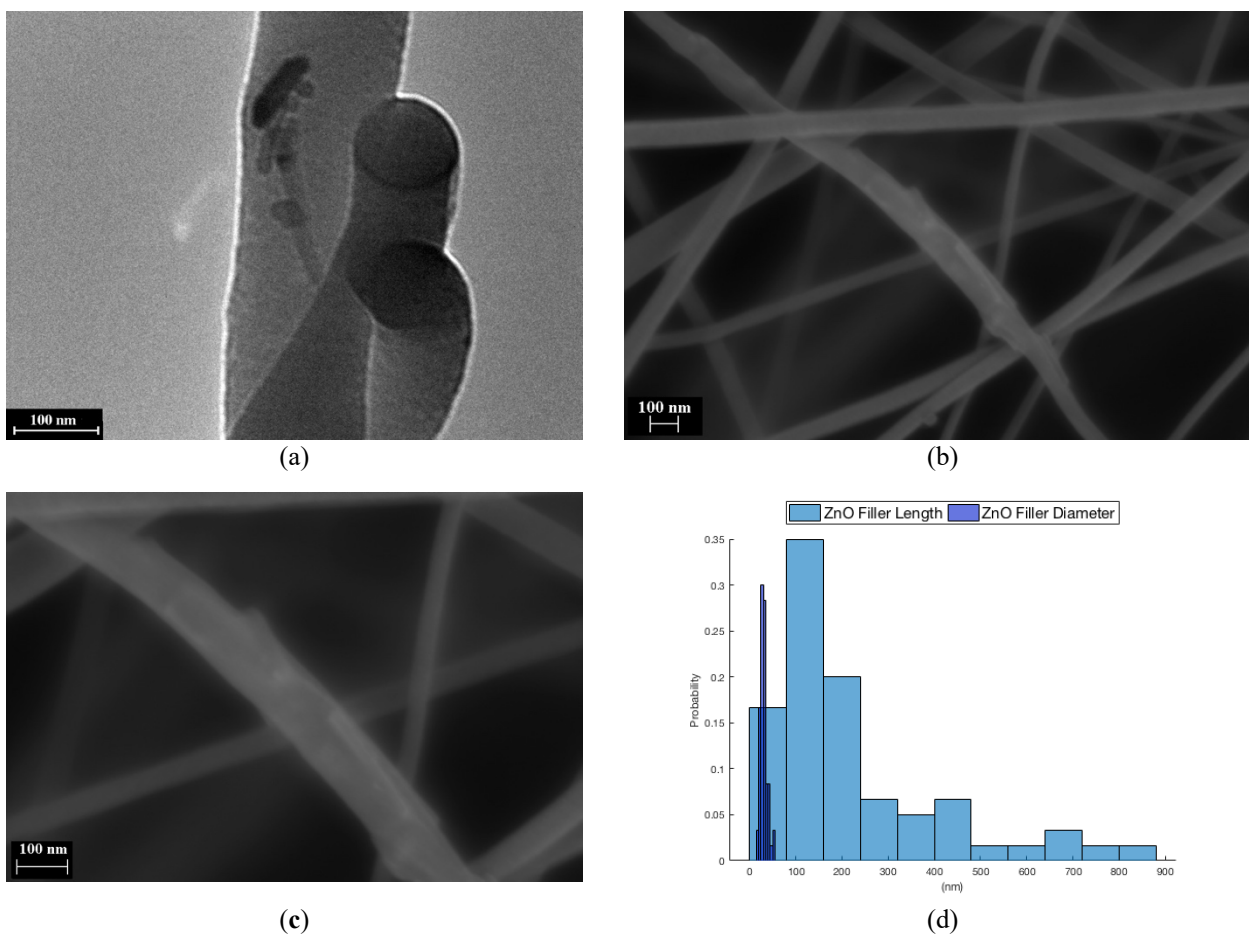


Figure 1. (a) A TEM image of the ZnO nanorod fillers in PVDF nanofibers; (b) an FESEM image of the ZnO nanorod fillers in PVDF nanofibers; (c) an enlarged image; and (d) a histogram of the diameter distribution of electrospun PVDF nanofibers.

The effect of adding ZnO nanorods in the PVDF electrospinning solution as fillers on the crystalline phases of PVDF nanofibers was studied with FTIR spectra (Figure 2). Each spectrum result was normalized by a signal of an internal standard at $1,454\text{ cm}^{-1}$ corresponding to the CH_2 in-plane bending.⁴⁵ Electrospun PVDF nanofibers, both with and without ZnO fillers, exhibited strong peaks corresponding to a polar β phase at 840 cm^{-1} (β , CH_2 rocking) and $1,276\text{ cm}^{-1}$ (β , CF out-of-plane deformation). Relatively weak non-polar, α -phase crystalline peaks were observed at 614 cm^{-1} (α , CF_2 bending, and skeletal bending), 762 cm^{-1} (α , CF_2 bending), 796 cm^{-1} (α , CF_2 rocking), and 975 cm^{-1} (α , CH out-of-plane deformation).^{46,47} The addition of ZnO nanorod fillers did not have a significant impact on polar β crystalline or non-polar, α -phase crystalline. This indicates that the ZnO nanorod fillers did not disrupt the crystallization of the PVDF polymers. Furthermore, the β -phase percentage was calculated using the following equation:

$$F_{\beta} = \frac{X_{\beta}}{X_{\alpha} + X_{\beta}} = \frac{A_{\beta}}{(K_{\beta}/K_{\alpha})A_{\alpha} + A_{\beta}} \quad (1)$$

where F_{β} represents the PVDF β -phase percentage, A_{α} and A_{β} denote their absorption bands at 762 and 840 cm^{-1} , and K_{α} and K_{β} are the absorption coefficients at the

respective wavenumbers, which are 6.1×10^4 and 7.7×10^4 $\text{cm}^2 \cdot \text{mol}^{-1}$, respectively.⁴⁷⁻⁴⁹ The calculated β -phase percentage for the electrospun PVDF nanofibers was 83.7%, and for the ZnO+PVDF nanofibers, it was 78.2%.

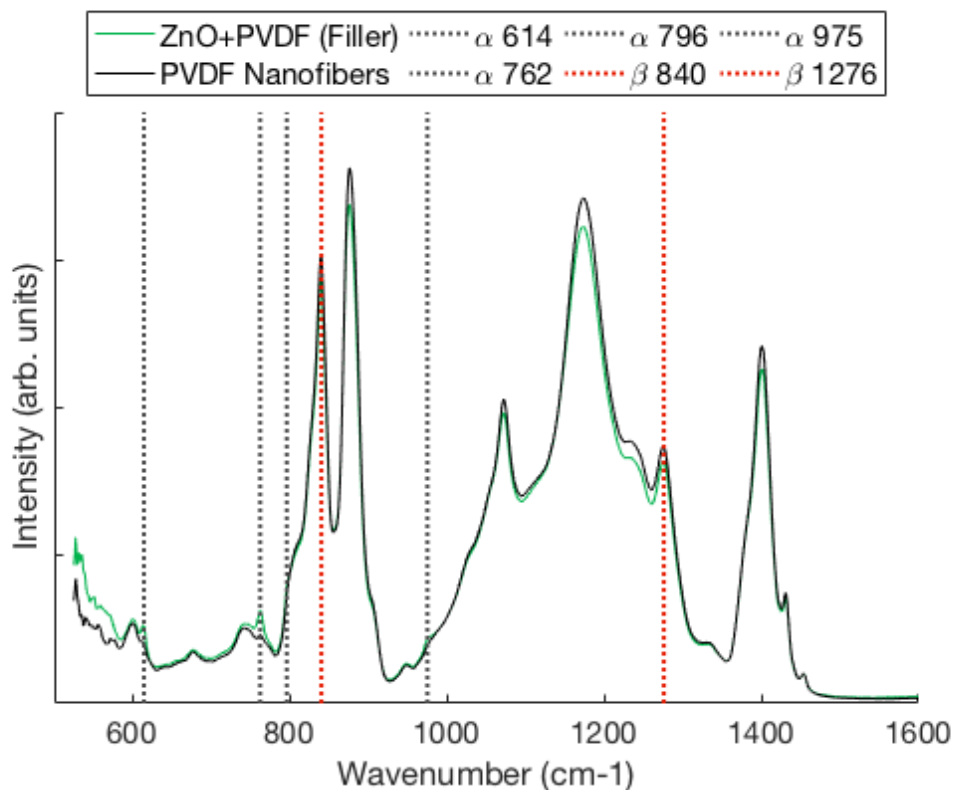


Figure 2. FTIR spectra showing the effect of the addition of ZnO nanorod fillers to PVDF crystalline phases.

The amount of ZnO added as fillers in the spinning solution accounted for 5 wt% of PVDF. The weight percentage of ZnO in the ZnO+PVDF composite was evaluated by TGA (Figure 3). The composite sample contained about 6.23 wt% of ZnO.

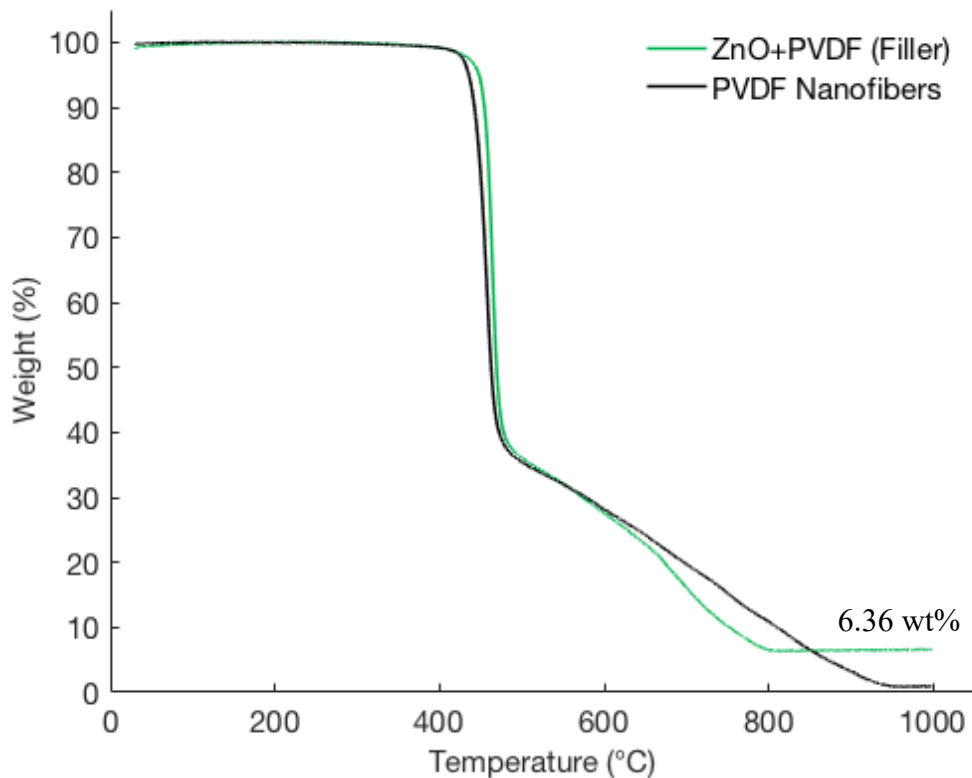


Figure 3. TGA of the PVDF membrane and ZnO+PVDF.

Figure 4 illustrates the X-ray diffraction patterns of the electrospun PVDF nanofibers and ZnO+PVDF composite nanofibers. The electrospun PVDF nanofibers exhibited strong peak 2θ values at 20.4° , which correspond to the β -phase crystalline. Moreover, ZnO/PVDF composite nanofibers have three reflection peaks at 2θ values of 31.9° (100), 34.5° (002), 36.4° (101), 47.7° (102), 56.8° (110), 63.1° (103), and 66.7° (112), which can be indexed as the hexagonal wurtzite structure.^{50,51} No diffraction peaks from any other impurity phases were found, confirming that only single-phase hexagonal ZnO was present. Peaks corresponding to the (100), (002), (101), (102), (110), (103), and (112) planes of ZnO+PVDF composite fibers confirmed the hydrothermal synthesis

of ZnO wurtzite crystals.^{52,53} There was no significant difference in the PVDF α and β crystalline peaks, with or without ZnO fillers, which corresponds with the FTIR spectra results.

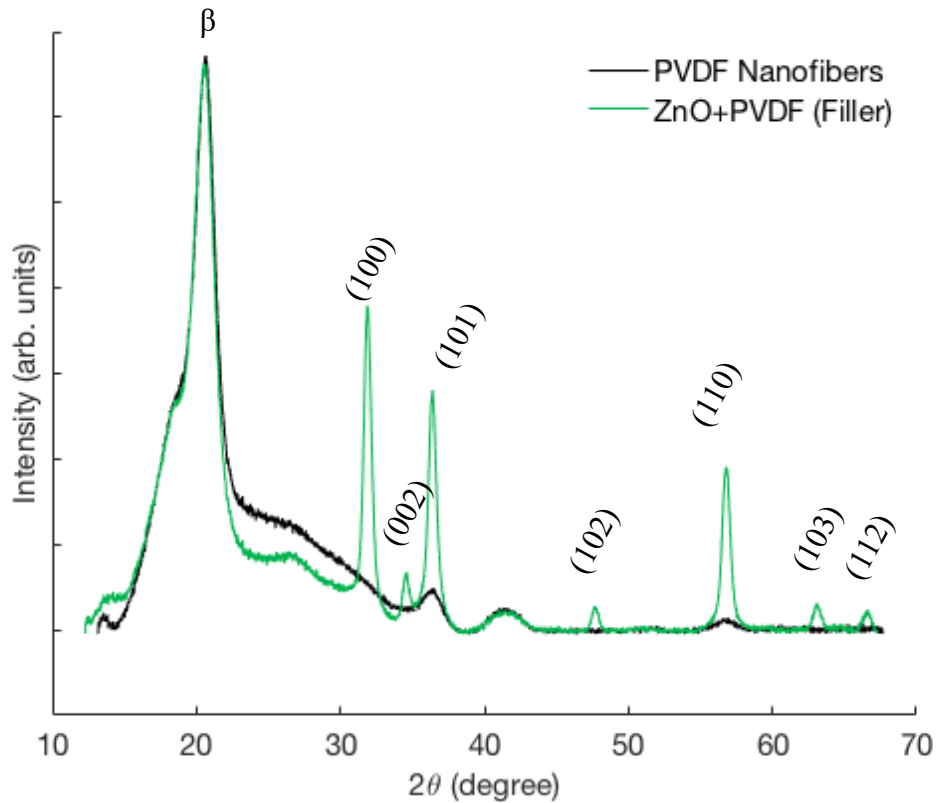


Figure 4. XRD spectra of the PVDF membrane and ZnO+PVDF.

2.3.2. Piezoelectric Measurements

The piezoelectric testing module of the ZnO+PVDF composite was assembled by sandwiching the piezoelectric nanofiber mat between two electrodes made by

conductive fabric. Figure 5 shows a schematic illustration of the breathable fibrous nanogenerator, which consists of a piezoelectric nanofiber membrane.

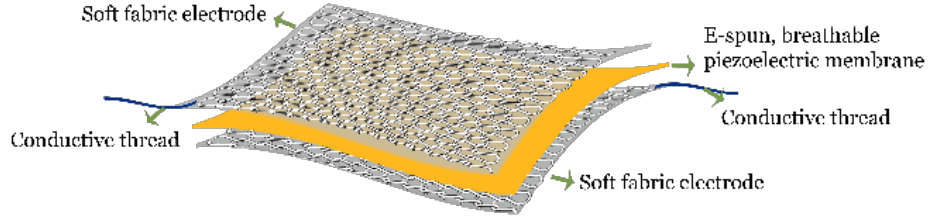


Figure 5. The schematic illustration of the breathable fibrous nanogenerator.

The closed-circuit currents of the nanogenerators with different resistive loads were compared, and the closed-circuit voltages and the power density were derived accordingly. Table 1 contains a list of the average values of the maximum peak currents with resistive loads of 0.47, 15, 30, and 60 M Ω . Figure 6a shows the nanogenerator load curve with all the data points from the different loads. Nonlinear least-square fitting was performed using the following equation:

$$V = V_{oc}(1 - \exp((I - I_{sc})/I_0)) \quad (2)$$

where V represents the measured voltage, I denotes the measured current, and V_{oc} , I_{sc} , and I_0 are the extracted parameters of the open-circuit voltage, short-circuit current, and I-V sharpness fitting, respectively. Figure 6b illustrates the typical transient current responses when the sample was subjected to cyclic compressive impacts with a resistive load of 15 M Ω .

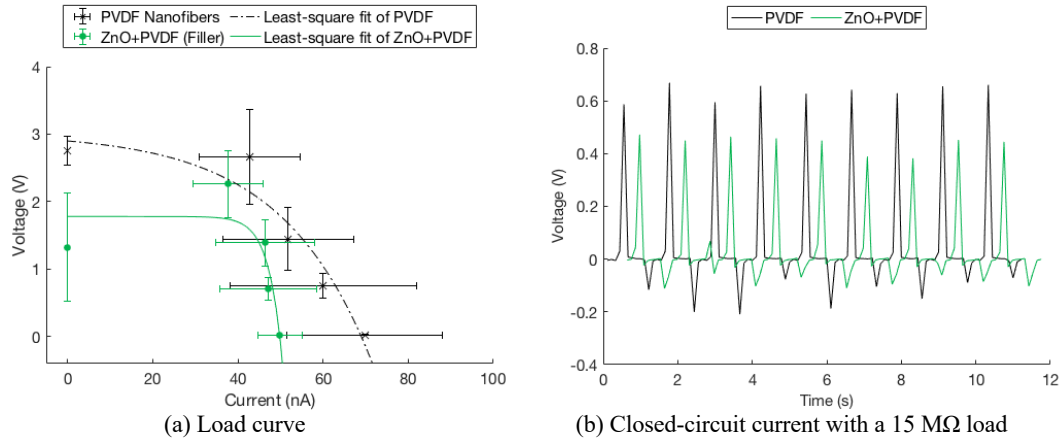


Figure 6. Nanogenerator characteristics of PVDF and ZnO+PVDF 15 cm² fiber mats: (a) load curves with resistive loads of 0.47, 15, 30, and 60 M Ω ; and (b) transient closed-circuit current measurements with a 15 M Ω resistive load.

Table 1. Measured closed-circuit current and voltage averages with conductive-knit electrodes.

		0.47 M Ω	15 M Ω	30 M Ω	60 M Ω
PVDF	Current (nA)	54.01	50.26	48.25	44.36
	Power Density (nW/cm ²)	0.09	2.53	4.66	7.87
	Voltage (V)	0.025	0.754	1.447	2.661
	Standard Deviation σ (V)	0.007	0.190	0.470	0.708
	Coefficient of Variation	0.29	0.25	0.32	0.27
ZnO+PVDF	Current (nA)	49.91	47.10	46.35	37.70
	Power Density (nW/cm ²)	0.08	2.22	4.30	5.69
	Voltage (V)	0.023	0.706	1.391	2.262
	Standard Deviation σ (V)	0.002	0.172	0.348	0.495
	Coefficient of Variation	0.10	0.24	0.25	0.22

As seen in Table 1 and Figure 6, ZnO+PVDF nanogenerators produced lower power output than PVDF nanogenerators under most of the load conditions. The addition of ZnO nanorods as fillers of the electrospinning solution of PVDF decreased open-circuit voltage by 50 % and closed-circuit voltage by 10 %, 10 %, 0 %, and 10 % with resistive loads of 470 k Ω , 15 M Ω , 30 M Ω , and 60 M Ω , respectively.

2.4. Conclusions

This study demonstrated that the addition of ZnO nanorods as fillers for PVDF nanofibers significantly decreases piezoelectric response as much as 50 % regarding open-circuit voltage. The addition of ZnO fillers does not weaken the polarization of PVDF created during electrospinning. However, the composite material did not exhibit a stronger piezoelectric response due to the addition of the ZnO nanorods as fillers.

CHAPTER 3. THE GROWTH OF ZNO NANORODS ON PVDF NANOFIBER SURFACES

3.1. Introduction

Contrary to the researcher's expectations, the composite material of ZnO nanorods and PVDF nanofibers by using ZnO as fillers reduced the piezoelectricity. In this chapter, the hydrothermal growth method of ZnO nanorods on the surface of PVDF fibers is presented in terms of the composite piezoelectricity.

3.2. Materials and Methods

3.2.1. Electrospinning of PVDF Nanofiber Mats

Initially, PVDF nanofiber mats were fabricated by electrospinning. The polymer solution of 20 wt% of PVDF ($M_w = 180,000$, Millipore Sigma, Burlington, MA, USA) was prepared with N,N-dimethylformamide (DMF, Macron Fine Chemicals, Center Valley, PA, USA) and acetone (Fisher Chemical, Waltham, MA, USA). The PVDF solution was prepared by adding PVDF pellets to the DMF–acetone solvent mixture (7/3 v/v) and then stirred with a magnetic stir bar on a hotplate at 70°C and 150 rpm for 3 h. The PVDF solution was drawn into a syringe with a spinneret needle with a gauge size of 23 and then pushed using a syringe pump (SK-500 III, Shenzhen Shenke Medical, Nanshan, China) with a rate of 1.0 mL/h. A high voltage of 14 kV was applied by a DC power supply (Matsusada Precision, Kusatsu-shi, Japan) to the needle. Fibers were accumulated on a grounded 100-mm-diameter collector rotating at 200 rpm. The distance between the cylindrical collector and spinneret was 10 cm. A Teflon tube was

used to connect the syringe and the needle, and the needle was moved laterally with a stroke of 18 cm and four strokes per min to obtain wide and uniform nanofiber mats.

3.2.2. Hydrothermal Growth of ZnO Nanorods

The hydrothermal growth method of ZnO nanorods on PVDF nanofiber was modified from a similar growth method on cotton or nylon microfibers.^{30,54-56} First, a solution concentration was diluted more than those in previously reported methods, resulting in smaller nanorods that would be in the range of nanofiber diameter. Second, the seeding step was repeated three times to produce nucleation sites on a more chemically inert PVDF fiber surface than nylon or cotton.⁵⁶ Third, the reaction temperature was lowered to 60°C to prevent the heat relaxation of semi-crystalline PVDF nanofibers.⁵⁷ Finally, equimolar amounts of hexamethylenetetramine and zinc nitrate hexahydrate in the growth solution were replaced by a higher concentration of hexamethylenetetramine to yield the preferred ratio of the length to diameter of ZnO crystals.^{55,58}

ZnO Seed Solution

The seed solution was prepared in 50 mM concentration and diluted to 10 mM before use. Zinc acetate dihydrate ($\text{Zn}(\text{Ac})_2 \cdot 2\text{H}_2\text{O}$, 1.6462 g) was dissolved in 150 mL of isopropyl alcohol at 85°C with a vigorous stir at 1,000 rpm for 17 min. Triethylamine ($\text{N}(\text{CH}_2\text{CH}_3)_3$, 0.7637 g) was added dropwise to the solution and stirred again at 85°C and 400 rpm for 13 min. The resulting 50 mM seed solution was incubated at room temperature without stirring for 6 h.⁵⁹

ZnO Growth Solution

The growth solution was prepared in 100 mM concentration and diluted to 10 mM before use. Hexamethylenetetramine ($C_6H_{12}N_4$, 9.3457 g) was dissolved in 400 mL of room-temperature deionized (DI) water, and the solution was stirred for 10 min. Zinc nitrate hexahydrate ($Zn(NO_3)_2$, 11.8991 g) was added to the solution and stirred for 24 h.⁵⁹

Growth of ZnO Nanorods on PVDF Fiber Surfaces

The successful growth of ZnO nanorods on cellulose or nylon fiber surfaces was achieved in previous research studies.^{17,30,54} Chemically, PVDF is more inert than cellulose or nylon, with more difficult seeding processes and fewer nucleation sites. During the seeding step of ZnO deposition, the seeding is critical to form hexagonal nanorods arranged vertically to the substrate surface for the maximum strain rate transfer.⁵⁴ Therefore, the seeding process was repeated three times to provide sufficient nucleation sites.^{56,59} The oven temperature for seed curing and growth process was lowered to 60°C to inhibit the heat relaxation of PVDF and preserve the piezoelectric polarization of the electrospun fibers, thus avoiding an additional poling process.⁵⁷ Equimolar amounts of hexamethylenetetramine and zinc nitrate hexahydrate in the growth solution were replaced by a higher concentration of hexamethylenetetramine to yield the preferred ratio of the polar and non-polar surface of ZnO crystals for higher piezoelectric responses.^{55,58}

3.2.3. Characterization

Field-emission scanning electron microscope (FESEM) images were taken using an LEO 1550 microscope (ZEISS, Oberkochen, Germany) with an accelerating voltage of

3 keV. To extract the detailed geometry with better focus and to reduce the charging effect under an FESEM, the samples were partially sputter coated with palladium/gold. The average PVDF fiber diameter and ZnO nanorod length and diameter were determined by analyzing FESEM images over 30 fibers with the ImageJ software (NIH, Bethesda, Rockville, MD, USA).⁴¹

The crystallography of PVDF nanofibers and ZnO nanorods was examined by X-ray diffraction (XRD) with the powder diffractometer (D8 GADDS, Bruker), and Cu-K α radiation (= 1.54 Å) at a 0.02° scanning step and an operating voltage of 40 kV and a current of 40 mA were used.

Fourier-transform infrared (FTIR) spectroscopy from 4,000 to 650 cm⁻¹ (Frontier FTIR, PerkinElmer, Waltham, MA, USA) was performed at room temperature to evaluate the polymer crystalline phase; FTIR spectra were collected with 16 scans and a resolution of 4 cm⁻¹.

Thermal gravimetric analyses (TGA) were used to determine the amount of ZnO added to PVDF nanofibers (Q500 Thermogravimetric Analyzer, TA Instruments, New Castle, DE, USA) by the heat removal of PVDF. Samples were heated up from room temperature to 990°C with the rate of 10°C/min on a ceramic pan under a nitrogen ambient.

3.2.4. Piezoelectric Testing

The piezoelectric testing module was assembled by sandwiching the piezoelectric nanofiber mat between two electrodes made by conductive fabric (cotton and silver

blend double jersey knit purchased from LessEMF, Latham, NY, USA). Wires were connected to the electrodes using conductive ink and epoxy.

The piezoelectric performance of the electrospun samples was evaluated by periodic tensile testing in a customized setup with a motorized actuator controlled by a controller and a module (ni-cRIO 9036 and ni-9503, National Instruments, Austin, TX, USA), a pressure sensor (LC201-300/N, Newport Electronics, Santa Ana, CA, USA), an electrometer (6517B, Keithley Instruments, Cleveland, OH, USA), a multimeter (34470A, Keysight, Santa Rosa, CA, USA), a source meter (2400, Keithley, Cleveland, OH, USA), and a programmable DC power supply (9130, BK Precision, Yorba Linda, CA, USA). The open-circuit voltage was measured with a Keithley 6517B electrometer, and the closed-circuit current was measured with a Keithley 2400 source meter. The testing head movement was set to 1 Hz, and the impact pressure was set to 0.10 MPa, which is within the human foot pressure range of 0–0.20 Mpa^{42–44}, although the applications are not limited to shoes. LabView software (National Instruments, Austin, TX, USA) was used to control all the components and to record voltage and current outputs synchronously.

3.3. Results and Discussion

Among piezoelectric polymers, PVDF has a high piezoelectric coefficient and is a semi-crystalline polymer with up to five different crystal phases (α , β , δ , γ , and ϵ).⁸ The two most common phases are the non-polar α phase (TGTG, trans-gauche) and the polar β phase (TTTT, all-trans).^{48,60} Among all phases, the β phase has the most favorable piezoelectric property, with the highest dipolar moment per unit cell.^{17,48} Many

researchers have conducted studies seeking to obtain a higher percentage of the β phase in PVDF. In terms of in-situ poling during fiber formation, drawing with an electric field during the melt spinning⁶⁰ and various types of electrospinning^{17,61–63} have been found to produce fibers with a high β -phase percentage. With electrospinning, the post-processing poling step is not necessarily due to the high field within the process. The resulting nanofiber mats also have large surface areas due to the small fiber diameters involved.⁶⁴

3.3.1. Material Analysis

The nanostructures of PVDF nanofibers and ZnO nanorods were first examined under an FESEM. As described in the experimental section, 3.2.2. Hydrothermal Growth of ZnO Nanorods, the ZnO nanorods were grown on the PVDF fiber surface by the hydrothermal growth method. The FESEM image in Figure 7a illustrates the morphology and the size distribution of the electrospun PVDF nanofibers and ZnO nanorods. The ZnO growth method resulted in two sizes of nanorods. Smaller ZnO nanorods (Figure 7a) had an average length of 142 ± 110 nm and diameter of 35 ± 9 nm (Figure 7b). The electrospun PVDF nanofibers (Figure 7c) with random fiber alignment had an average diameter of 168 ± 113 nm (Figure 7d).

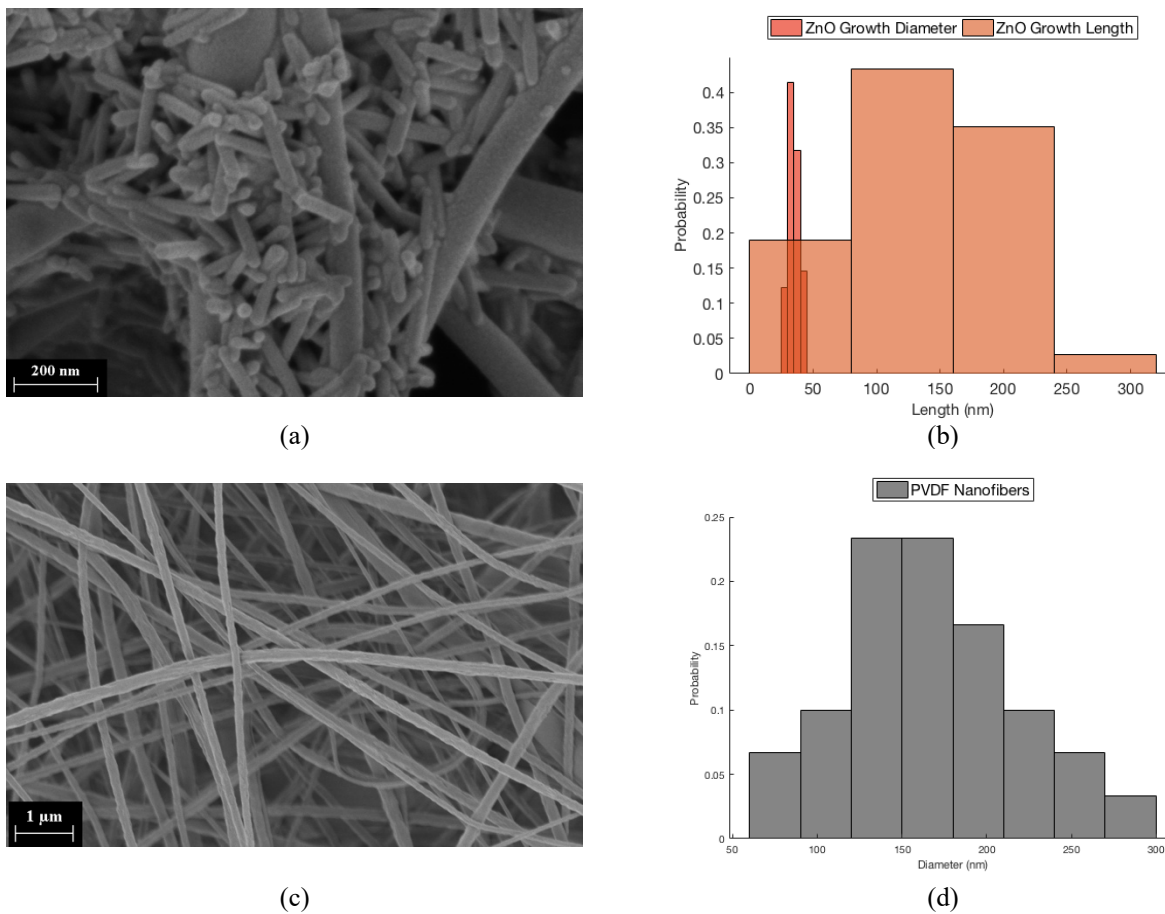


Figure 7. (a) An FESEM image of the smaller type ZnO nanorods grown on the surface of the electrospun PVDF nanofiber; (b) a histogram of the length and diameter distributions of the smaller ZnO nanorods; (c) an image of the electrospun PVDF nanofiber; and (d) a histogram of the diameter distribution of electrospun PVDF nanofibers.

Furthermore, FTIR spectra were studied to analyze the PVDF crystalline phases under the electrospinning and hydrothermal growth process. The FTIR spectra of the PVDF polymer pellets, electrospun PVDF nanofibers, and ZnO@PVDF nanofibers are compared in Figure 8. Each spectrum was normalized by a signal of an internal standard at $1,454\text{ cm}^{-1}$ corresponding to the CH_2 in-plane bending.⁴⁵ The pellet exhibits strong

peaks corresponding to non-polar, phase- α crystalline at 614 cm^{-1} (α , CF_2 bending and skeletal bending), 762 cm^{-1} (α , CF_2 bending), 796 cm^{-1} (α , CF_2 rocking), and 975 cm^{-1} (α , CH out-of-plane deformation).^{46,47} After electrospinning, peaks at 840 cm^{-1} (β , CH₂ rocking) and 1276 cm^{-1} (β , CF out-of-plane deformation) became stronger, and peaks corresponding to α crystalline became weaker. The hydrothermal growth of ZnO nanorods did not depolarize PVDF fibers, and similar FTIR spectra of nanofibers confirmed this before and after the growth process. The maintained intensity of β crystalline peaks indicates that PVDF polarization did not relax during hydrothermal growth. Furthermore, the β -phase percentage can be quantified using the following equation:

$$F_{\beta} = \frac{X_{\beta}}{X_{\alpha} + X_{\beta}} = \frac{A_{\beta}}{(K_{\beta}/K_{\alpha})A_{\alpha} + A_{\beta}} \quad (3)$$

where F_{β} represents the PVDF β -phase percentage, A_{α} and A_{β} denote their absorption bands at 762 and 840 cm^{-1} , and K_{α} and K_{β} are the absorption coefficients at the respective wavenumbers, which are 6.1×10^4 and $7.7 \times 10^4 \text{ cm}^2 \cdot \text{mol}^{-1}$, respectively.⁴⁷⁻⁴⁹ The calculated β -phase percentage for PVDF pellets was 49.3%; for the electrospun PVDF and the ZnO@PVDF nanofibers, it was 83.7% and 80.1%, respectively. The hydrothermal growth temperature of ZnO nanorods on PVDF fibers was set to 60°C, because, at higher temperatures, PVDF polymer tends to relax, reducing its piezoelectric responses. The Curie temperature, when the piezoelectric response of PVDF polymers vanishes, is about 165°C–170°C.⁵⁷ From the comparison of the three FTIR spectra, it can be concluded that the electrospinning process successfully produced PVDF fibers

with a high percentage of β phase, and ZnO nanorod growth did not depolarize the PVDF nanofibers.

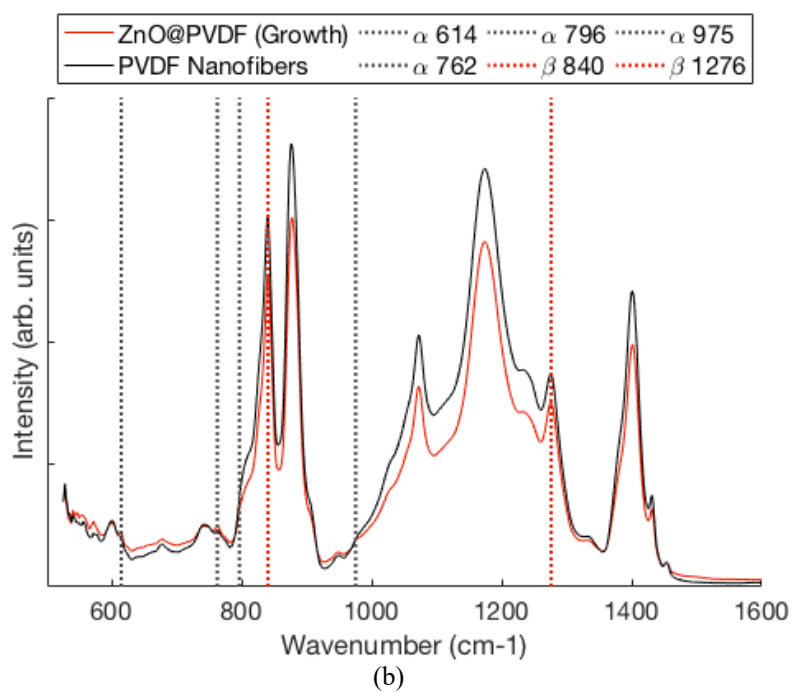
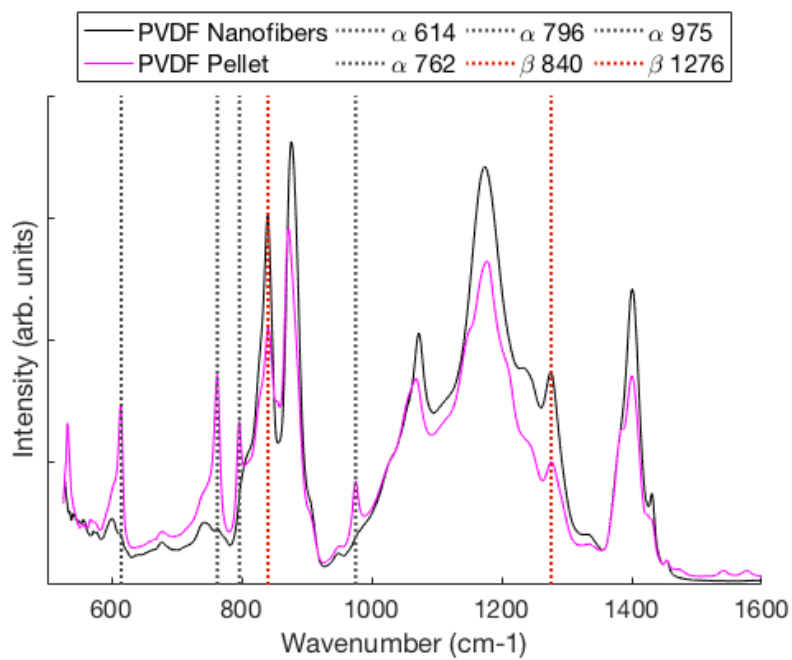


Figure 8. FTIR spectra showing the effect of (a) electrospinning and (b) hydrothermal growth of ZnO nanorods on PVDF crystalline phases.

Figure 9 displays the X-ray diffraction patterns of the PVDF pellet, electrospun PVDF nanofibers, and ZnO@PVDF composite nanofibers. The electrospun PVDF nanofibers exhibited strong peak 2θ values at 20.4° , which correspond to the β -phase crystalline. In addition, ZnO@PVDF composite nanofibers have four reflection peaks at 2θ values of 31.9° (100), 34.5° (002), 36.4° (101), and 56.8° (110), which can be indexed as the hexagonal wurtzite structure.^{50,51} The wurtzite structure is the most thermodynamically stable form of anisotropic hydrothermal growth owing to the presence of polar and non-polar surfaces, with a natural tendency to minimize the polar surface and surface energy.^{54,65} No diffraction peaks from any other impurity phases were found, confirming that only single-phase hexagonal ZnO was present. Peaks corresponding to the (100), (002), (101), and (110) planes of ZnO@PVDF composite fibers confirmed the hydrothermal growth of ZnO wurtzite crystals at 60°C .^{52,53} No notable difference between PVDF α and β crystalline peaks before and after hydrothermal ZnO growth was observed. Therefore, our hydrothermal growth at a relatively low temperature resulted in the successful growth of ZnO without depolarizing the electrospun piezoelectric nanofibers.

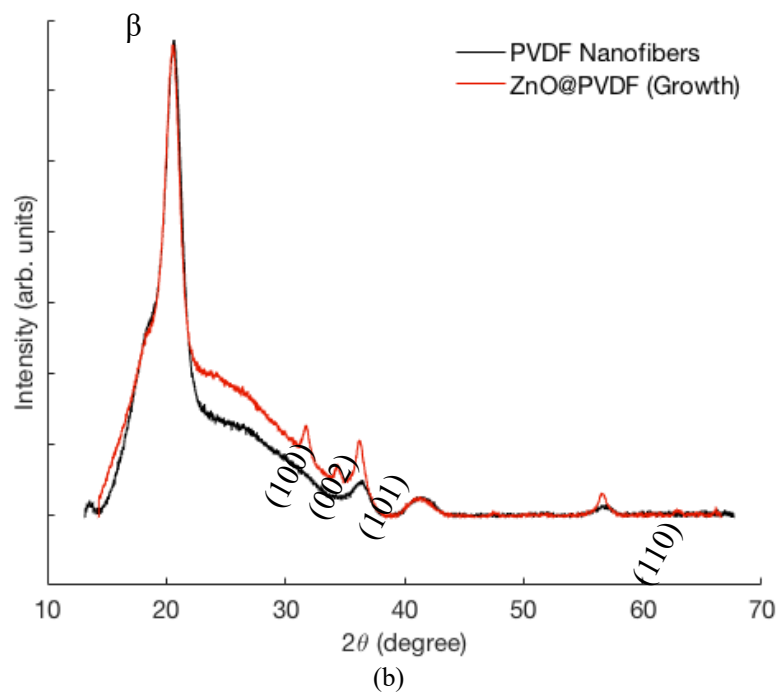
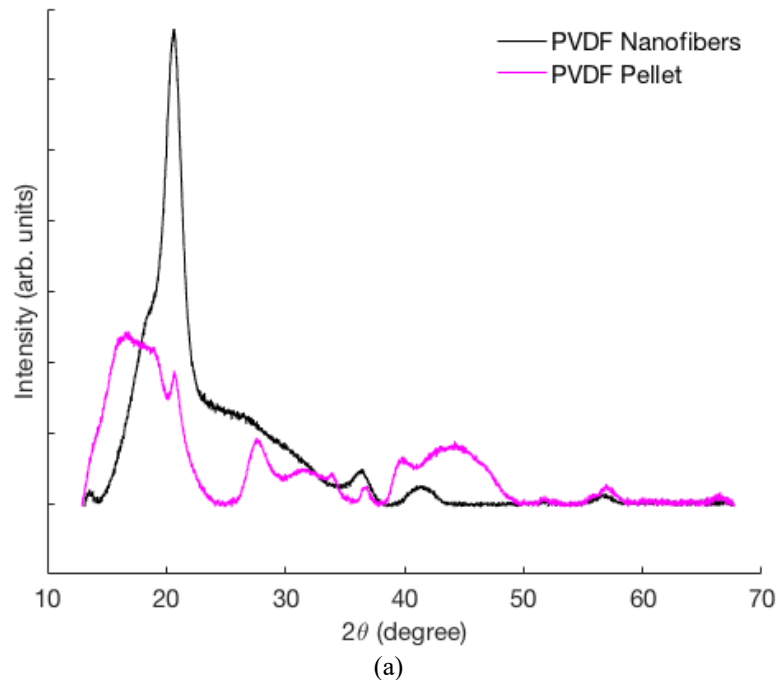


Figure 9. XRD spectra of the (a) PVDF pellet and PVDF nanofibers; and (b) the electrospun PVDF nanofibers before and after the hydrothermal growth of ZnO nanorods.

The amount of ZnO added to PVDF fibers was evaluated by TGA (Figure 10) and calculated by the weight loss of the samples at the end of the heating cycle. The composite sample contained about 6.23 wt% of ZnO. The ZnO weight percentage in the composite was relatively small because ZnO nanorod growth is limited to the surface of the nanofiber membrane.

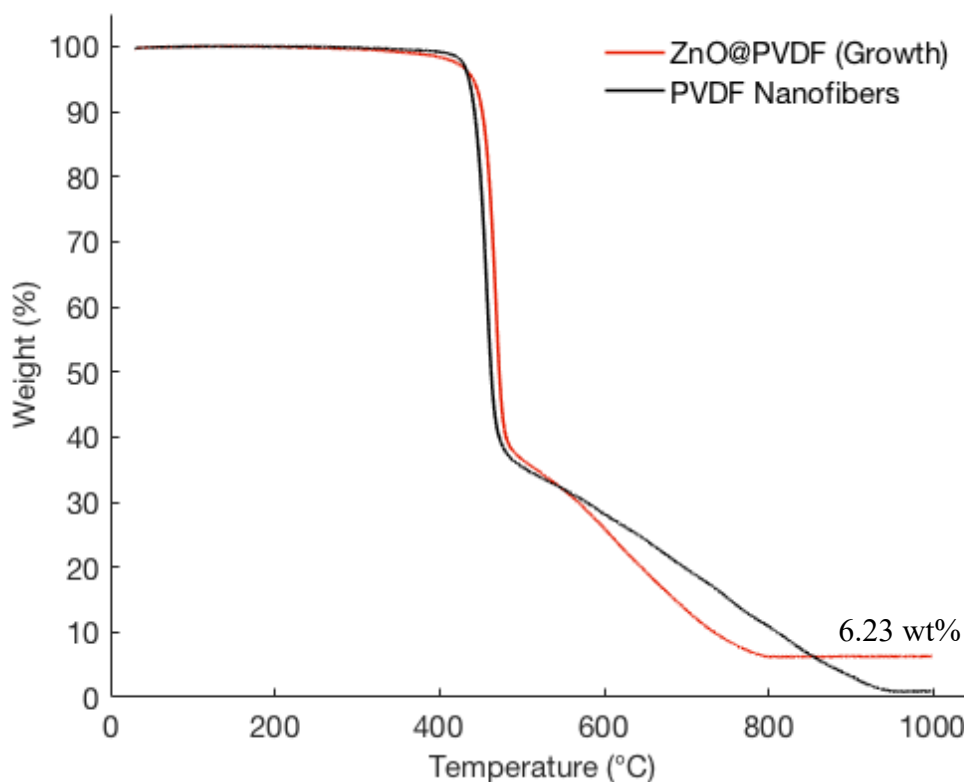


Figure 10. TGA of the PVDF membrane and ZnO@PVDF.

3.3.2. Piezoelectric Measurements

The piezoelectric testing module of the ZnO@PVDF composite was assembled by sandwiching the piezoelectric nanofiber mat between two electrodes made by conductive fabric.

The closed-circuit currents of the nanogenerators with different resistive loads were compared, and the closed-circuit voltages and the power density were derived accordingly. Table 2 lists the average values of the maximum peak currents with resistive loads of 0.47, 15, 30, and 60 MΩ. Figure 11a displays the nanogenerator load curve with all the data points from the different loads. Nonlinear least-square fitting was performed using the following equation:

$$V = V_{oc}(1 - \exp((I - I_{sc})/I_0)) \quad (4)$$

where V represents the measured voltage, I denotes the measured current, and V_{oc} , I_{sc} , and I_0 are the extracted parameters of the open-circuit voltage, short-circuit current, and I - V sharpness fitting. Figure 11b illustrates the typical transient current responses when the sample was subjected to cyclic compressive impact with a resistive load of 15 MΩ.

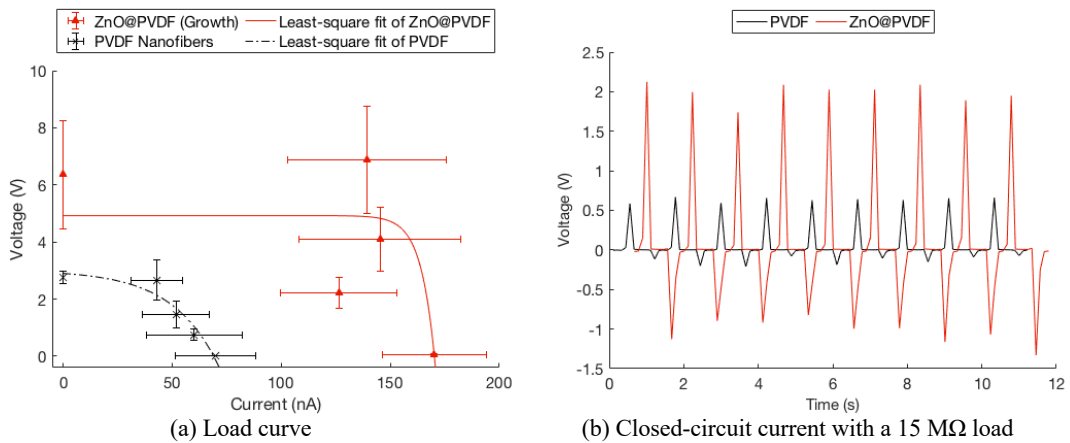


Figure 11. Nanogenerator characteristics of PVDF and ZnO@PVDF 15 cm² fiber mats: (a) load curves with resistive loads of 0.47, 15, 30, and 60 MΩ; and (b) transient closed-circuit current measurements with a 15 MΩ resistive load.

Table 2. Measured closed-circuit current and voltage averages with conductive-knit electrodes.

		0.47 MΩ	15 MΩ	30 MΩ	60 MΩ
PVDF	Current (nA)	54.01	50.26	48.25	44.36
	Power Density (nW/cm ²)	0.09	2.53	4.66	7.87
	Voltage (V)	0.025	0.754	1.447	2.661
	Standard Deviation σ (V)	0.007	0.190	0.470	0.708
	Coefficient of Variation	0.29	0.25	0.32	0.27
ZnO@PVDF	Current (nA)	136.88	147.66	136.69	114.67
	Power Density (nW/cm ²)	0.59	31.80	37.37	52.60
	Voltage (V)	0.064	2.215	4.101	6.880
	Standard Deviation σ (V)	0.016	0.553	1.111	1.886
	Coefficient of Variation	0.25	0.25	0.27	0.27

As seen in Table 2 and Figure 11, ZnO@PVDF nanogenerators produced significantly higher power output than PVDF nanogenerators under all load conditions. Growing ZnO nanorods on the surface of the electrospun PVDF nanofibers increased open-circuit voltage by 130 % and closed-circuit voltage by 150 %, 190 %, 180 %, and 160 % with resistive loads of 470 kΩ, 15 MΩ, 30 MΩ, and 60 MΩ, respectively.

3.4. Conclusions

This study demonstrated that the piezoelectric responses of PVDF fibrous nanogenerators could be significantly enhanced by least 130 % regarding open-circuit voltage by growing ZnO nanorods on PVDF fibers via a low-temperature hydrothermal process that did not weaken the polarization of PVDF created during electrospinning.

CHAPTER 4. ELECTROSPRAYING OF ZNO NANORODS ON THE SURFACE OF PVDF NANOFIBER MATS

4.1. Introduction

The growth of ZnO nanorods on the surface of the PVDF nanofibers successfully improved the piezoelectric response of the nanofiber mats without compromising the polar β phase of PVDF. Lowering the growth temperature to 60°C resulted in the successful growth of ZnO nanorods without depoling electrospun PVDF. However, the temperature was not high enough to control ZnO nanorod size and quantity.

The electrospaying method was studied as another way to add ZnO nanorods on the surface of PVDF nanofibers and to have more control over the ZnO amount and size.

4.2. Materials and Methods

4.2.1. Electrospinning of PVDF Nanofiber Mats

In this study, PVDF pellets (Mw 180,000, Millipore Sigma, Burlington, MA, USA), N,N-dimethylformamide (DMF, Macron Fine Chemicals, Radnor, PA, USA), and acetone (Fisher Chemical, Waltham, MA, USA) were used as received from the companies. Then, 20 wt% of PVDF solution was prepared by adding PVDF pellets to the DMF–acetone solvent mixture (7/3 v/v) and stirring the solution with a magnetic stirring bar at 70°C for 5 h. The polymer solution was loaded into a plastic syringe, and a 23-gauge needle was used as a spinneret. The flow rate was controlled at 1 mL/h with a syringe pump (PHD ULTRA, Harvard Apparatus), and a 14 kV voltage was applied by a DC power supply (Matsusada Precision) between the needle and a grounded metal collector with a distance of 10 cm. The needle was moved laterally with a stroke distance

of 18 cm and four strokes per min. The collector was 10 cm in diameter, and the rotation speed was 200 rpm.⁵⁹

4.2.2. Hydrothermal Synthesis of ZnO Nanorods

Single-crystalline ZnO nanorods with small diameters were prepared by the hydrothermal synthesis method in an autoclave. Then, 20 mL of 0.1 M of a zinc acetate dihydrate ($\text{Zn}(\text{Ac})_2 \cdot 2\text{H}_2\text{O}$) solution in ethanol and 40 mL of 0.5 M sodium hydroxide (NaOH) in ethanol was transferred to a Teflon-lined stainless steel autoclave and heated at 150°C for 15 h.⁴⁰ The solution with white precipitate was vacuum filtered with 0.4 μm membranes.

4.2.3. Electrospaying of ZnO Nanorods onto PVDF Nanofiber Mats

In this study, 10 mL of 1.5 wt% ZnO nanorods in water was sonicated for 90 min and then electrospayed onto PVDF nanofiber mats on the collector. The flow rate was 10 mL/h, and the rest of the parameters were the same as those used in the electrospinning process for PVDF.

4.2.4. Characterization

Field-emission scanning electron microscope (FESEM) images were taken using a Gemini 500 microscope (ZEISS, Oberkochen, Germany) with an accelerating voltage of 1 keV. To extract the detailed geometry with better focus and to reduce the charging effect under an FESEM, the samples were partially sputter coated with palladium/gold. The average PVDF fiber diameter and ZnO nanorod length and diameter were

determined by analyzing FESEM images over 30 fibers with the ImageJ software (NIH, Bethesda, Rockville, MD, USA).⁴¹

The crystallography of PVDF nanofibers and ZnO nanorods was examined by X-ray diffraction (XRD) with the powder diffractometer (D8 GADDS, Bruker), and Cu-K α radiation ($\lambda = 1.54 \text{ \AA}$) at a 0.02° scanning step and an operating voltage of 40 kV and a current of 40 mA were used.

Fourier-transform infrared (FTIR) spectroscopy from 4,000 to 650 cm^{-1} (Frontier FTIR, PerkinElmer, Waltham, MA, USA) was performed at room temperature to evaluate the polymer crystalline phase. In addition, FTIR spectra were collected with 16 scans and a resolution of 4 cm^{-1} .

Thermal gravimetric analyses (TGA) were used to determine the amount of ZnO added to PVDF nanofibers (Q500 Thermogravimetric Analyzer, TA Instruments, New Castle, DE, USA) by the heat removal of PVDF. Samples were heated up from room temperature to 990°C with the rate of 10°C/min on a ceramic pan under a nitrogen ambient.

4.2.5. Piezoelectric Testing

The piezoelectric testing module was assembled by sandwiching the piezoelectric nanofiber mat between two electrodes made by conductive fabric (cotton and silver blend double jersey knit purchased from LessEMF, Latham, NY, USA). Wires were connected to the electrodes using conductive ink and epoxy.

The piezoelectric performance of the electrospun samples was evaluated by periodic tensile testing in a customized setup with a motorized actuator controlled by a controller

and a module (ni-cRIO 9036 and ni-9503, National Instruments, Austin, TX, USA), a pressure sensor (LC201-300/N, Newport Electronics, Santa Ana, CA, USA), an electrometer (6517B, Keithley Instruments, Cleveland, OH, USA), a multimeter (34470A, Keysight, Santa Rosa, CA, USA), a source meter (2400, Keithley, Cleveland, OH, USA), and a programmable DC power supply (9130, BK Precision, Yorba Linda, CA, USA). The open-circuit voltage was measured with a Keithley 6517B electrometer, and the closed-circuit current was measured with a Keithley 2400 source meter. The testing head movement was set to 1 Hz, and the impact pressure was set to 0.10 MPa, which is within the human foot pressure range of 0–0.20 MPa,^{42–44}, although the applications are not limited to shoes. LabView software (National Instruments, Austin, TX, USA) was used to control all the components and to record voltage and current outputs synchronously.

4.3. Results and Discussion

The effect of electrospaying nanofibers on the surface of PVDF fibers were studied, such as morphology, PVDF β phase, crystallinity, and piezoelectricity.

4.3.1. Material Analysis

The morphology of ZnO nanorods electrospayed on the PVDF surface (ZnO/PVDF) was examined using an FESEM. Figure 12 shows the morphology, the size distribution of ZnO nanorod diameter, and the nanorod length. Figure 12a illustrates the morphology of ZnO/PVDF, and Figure 12b displays the distribution of diameter and length of ZnO nanorods (Figure 12d), which had an average diameter of 31 ± 22 nm and length of 228 ± 613 nm.

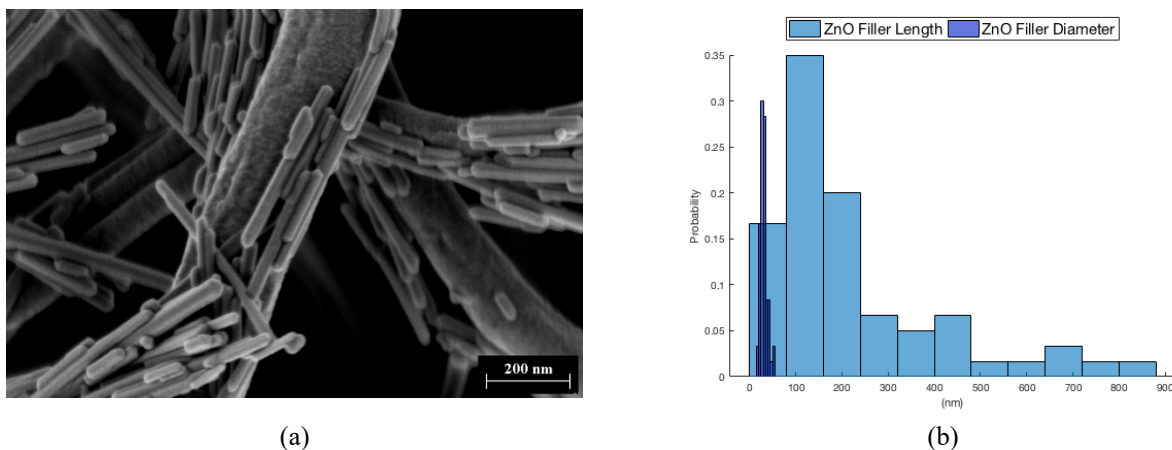


Figure 12. (a) An FESEM image of the ZnO nanorods electrospayed on the surface of the electrospun PVDF nanofiber (ZnO/PVDF); and (b) a histogram of the length and diameter distributions of ZnO nanorods.

The effect of electrospaying ZnO nanorods on the crystalline phases of PVDF nanofibers was studied with FTIR spectra (Figure 13). Each spectrum was normalized by a signal of an internal standard at $1,454\text{ cm}^{-1}$ corresponding to the CH_2 in-plane bending.⁴⁵ Electrospun PVDF nanofiber exhibits strong peaks corresponding to the polar β phase at 840 cm^{-1} (β , CH_2 rocking) and $1,276\text{ cm}^{-1}$ (β , CF out-of-plane deformation). After electrospaying ZnO nanorods on the surface of PVDF nanofiber mats, peaks corresponding to non-polar, α -phase crystalline had a slight increase at 614 cm^{-1} (α , CF_2 bending and skeletal bending), 762 cm^{-1} (α , CF_2 bending), 796 cm^{-1} (α , CF_2 rocking), and 975 cm^{-1} (α , CH out-of-plane deformation).^{46,47} This indicates that the electrospaying of ZnO nanorods did slightly depolarize the PVDF fibers. Furthermore, the β -phase percentage was calculated using the following equation:

$$F_{\beta} = \frac{X_{\beta}}{X_{\alpha} + X_{\beta}} = \frac{A_{\beta}}{(K_{\beta}/K_{\alpha})A_{\alpha} + A_{\beta}} \quad (5)$$

where F_{β} represents the PVDF β -phase percentage, A_{α} and A_{β} denote their absorption bands at 762 and 840 cm^{-1} , and K_{α} and K_{β} are the absorption coefficients at the respective wavenumbers, which are 6.1×10^4 and $7.7 \times 10^4 \text{ cm}^2 \cdot \text{mol}^{-1}$, respectively.⁴⁷⁻⁴⁹ The calculated β -phase percentage for the electrospun PVDF and ZnO/PVDF nanofibers was 83.7% and 67.8%, respectively.

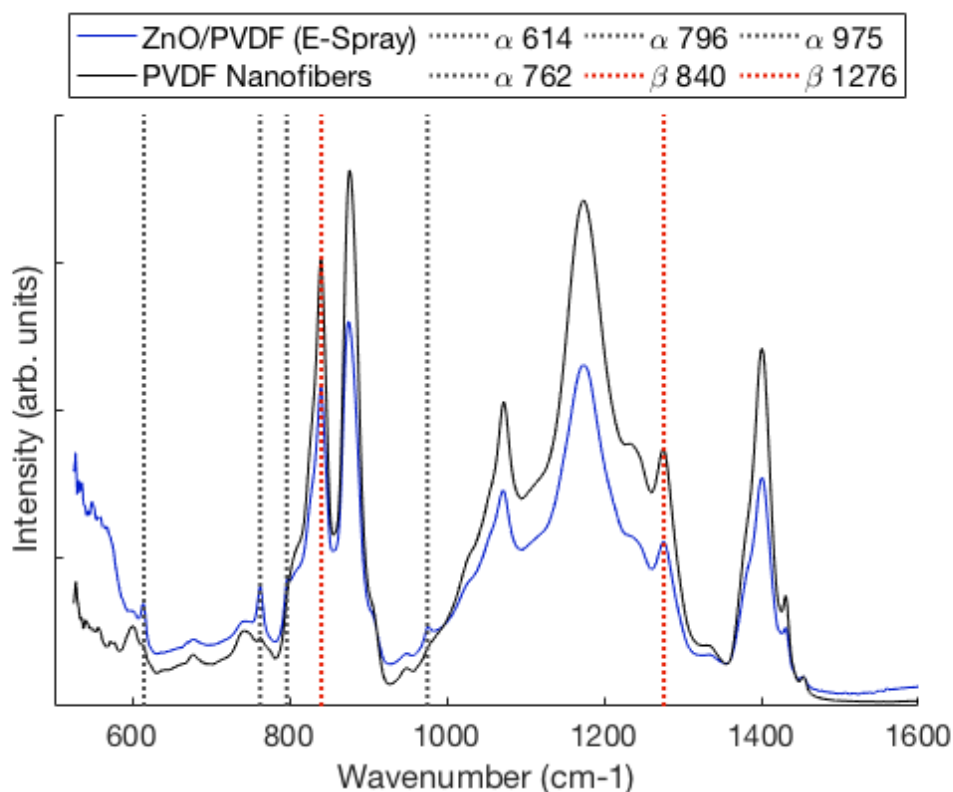


Figure 13. FTIR spectra showing the effect of electrospaying of ZnO nanorods on PVDF crystalline phases.

The amount of ZnO added onto PVDF fibers by electrospaying was evaluated by TGA (Figure 14) and calculated by the weight loss of the samples at the end of the heating cycle. The composite sample contained about 6.36 wt% of ZnO. The ZnO addition amount was controlled to be close to the ZnO growth method for comparison.

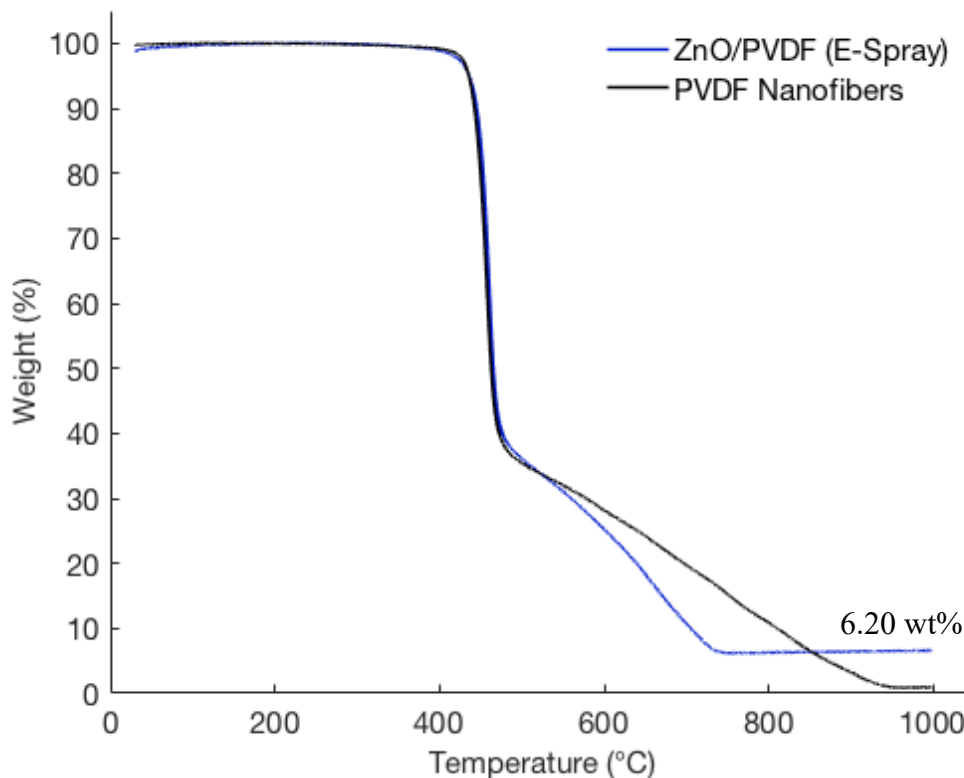


Figure 14. TGA of the PVDF membrane and ZnO/PVDF.

Figure 15 shows the X-ray diffraction patterns of the electrospun PVDF nanofibers and ZnO/PVDF composite nanofibers. The electrospun PVDF nanofibers exhibited strong peak 2θ values at 20.4° , which correspond to the β -phase crystalline. In addition, ZnO/PVDF composite nanofibers have three reflection peaks at 2θ values of 31.9° (100), 34.5° (002), 36.4° (101), 47.7° (102), 56.8° (110), 63.1° (103), and 66.7° (112),

which can be indexed as the hexagonal wurtzite structure.^{50,51} No diffraction peaks from any other impurity phases were found, confirming that only single-phase hexagonal ZnO was present. Peaks corresponding to the (100), (002), (101), (102), (110), (103), and (112) planes of ZnO/PVDF composite fibers confirmed the hydrothermal synthesis of ZnO wurtzite crystals.^{52,53} The PVDF β crystalline peak became weaker after the electrospinning, which corresponds to the FTIR spectra.

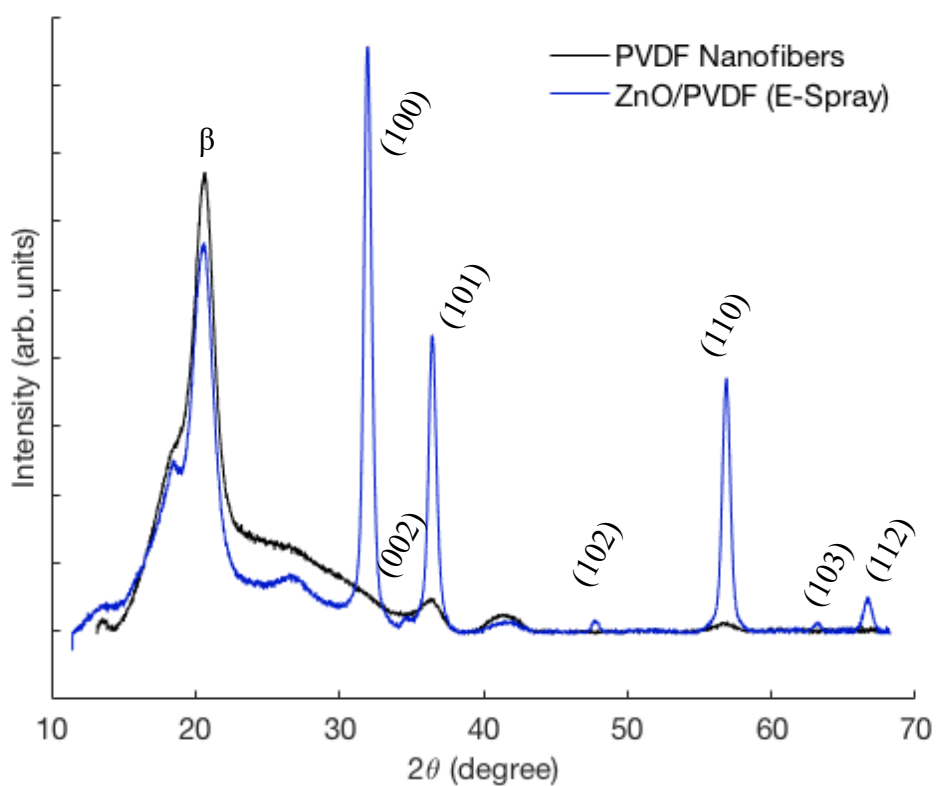


Figure 15. XRD spectra of the PVDF membrane and ZnO/PVDF.

4.3.2. Piezoelectric Measurement

The piezoelectric testing module of the ZnO/PVDF composite was assembled by sandwiching the piezoelectric nanofiber mat between two electrodes made by conductive fabric.

The closed-circuit currents of the nanogenerators with different resistive loads were compared, and the closed-circuit voltages and the power density were derived accordingly. Table 3 lists the average values of the maximum peak currents with resistive loads of 0.47, 15, 30, and 60 MΩ. Figure 16a shows the nanogenerator load curve with all the data points from the different loads. Nonlinear least-square fitting was performed using the following equation:

$$V = V_{oc}(1 - \exp((I - I_{sc})/I_0)) \quad (6)$$

where V represents the measured voltage, I denotes the measured current, and V_{oc} , I_{sc} , and I_0 are the extracted parameters of the open-circuit voltage, short-circuit current, and I-V sharpness fitting. Figure 16b depicts the typical transient current responses when the sample was subjected to cyclic compressive impact with a resistive load of 15 MΩ.

As seen in Table 3 and Figure 16, ZnO/PVDF nanogenerators produced significantly higher power output than PVDF nanogenerators under all load conditions. Electrospaying ZnO nanorods on the surface of the electrospun PVDF nanofibers increased open-circuit voltage by 390 %, and closed-circuit voltage by 152 %, 440 %, 500 %, and 460 % with resistive loads of 470 kΩ, 15 MΩ, 30 MΩ, and 60 MΩ, respectively.

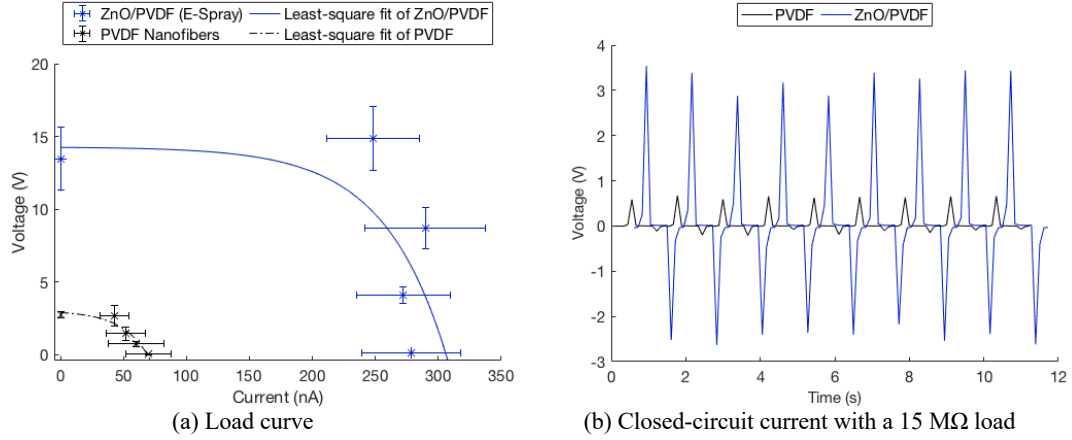


Figure 16. Nanogenerator characteristics of PVDF and ZnO/PVDF 15 cm² fiber mats: (a) load curves with resistive loads of 0.47, 15, 30, and 60 MΩ; and (b) transient closed-circuit current measurements with a 15 MΩ resistive load.

Table 3. Measured closed-circuit current and voltage averages with conductive-knit electrodes.

		0.47 MΩ	15 MΩ	30 MΩ	60 MΩ
PVDF	Current (nA)	54.01	50.26	48.25	44.36
	Power Density (nW/cm ²)	0.09	2.53	4.66	7.87
	Voltage (V)	0.025	0.754	1.447	2.661
	Standard Deviation σ (V)	0.007	0.190	0.470	0.708
	Coefficient of Variation	0.29	0.25	0.32	0.27
ZnO/PVDF	Current (nA)	278.26	272.19	289.62	247.81
	Power Density (nW/cm ²)	2.43	74.09	167.76	245.63
	Voltage (V)	0.131	4.083	8.689	14.868
	Standard Deviation σ (V)	0.018	0.560	1.430	2.205
	Coefficient of Variation	0.14	0.14	0.16	0.15

4.4. Conclusions

This study revealed that the piezoelectric responses of PVDF fibrous nanogenerators could be significantly enhanced by at least 390 % regarding open-circuit voltage by electrospaying ZnO nanorod on PVDF fibers. The process does slightly weaken the polarization of PVDF created during electrospinning. However, the composite material exhibits a strong piezoelectric response due to the addition of ZnO nanorods on the PVDF nanofiber mat surface.

CHAPTER 5. THE COMPARISON OF THREE TYPES OF PVDF AND ZNO NANOFIBROUS COMPOSITES

5.1. Introduction

Three ZnO and PVDF composite fabrication methods were studied: filler, growth, and electrospray in Chapters 2, 3, and 4, respectively. This chapter consists of a comparison of all three methods in terms of their material characteristics and piezoelectricity.

5.2. Materials and Methods

5.2.1. Electrospinning of PVDF Nanofiber Mats

In this study, PVDF pellets (Mw 180,000, Millipore Sigma, Burlington, MA, USA), N,N-dimethylformamide (DMF, Macron Fine Chemicals, Radnor, PA, USA), and acetone (Fisher Chemical, Waltham, MA, USA) were used as received from the companies. Then, 20 wt% of PVDF solution was prepared by adding PVDF pellets to the DMF–acetone solvent mixture (7/3 v/v) and stirring the solution with a magnetic stirring bar at 70°C for 5 h. The polymer solution was loaded into a plastic syringe, and a 23-gauge needle was used as a spinneret. The flow rate was controlled at 1 mL/h with a syringe pump (PHD ULTRA, Harvard Apparatus, Cambridge, MA, USA), and a 14 kV voltage was applied by a DC power supply (Matsusada Precision, Kusatsu-shi, Japan) between the needle and a grounded metal collector with a distance of 10 cm. The needle was moved laterally with a stroke distance of 18 cm and four strokes per min. The collector was 10 cm in diameter, and the rotation speed was 200 rpm.⁵⁹

5.2.2. Hydrothermal Synthesis of ZnO Nanorods

Single-crystalline ZnO nanorods with small diameters were prepared by the hydrothermal synthesis method in an autoclave. Then, 20 mL of 0.1 M of a zinc acetate dihydrate ($\text{Zn}(\text{Ac})_2 \cdot 2\text{H}_2\text{O}$) solution in ethanol and 40 mL of 0.5M sodium hydroxide (NaOH) in ethanol was transferred to a Teflon-lined stainless steel autoclave and heated at 150°C for 15 h.⁴⁰ The solution with white precipitate was vacuum filtered with 0.4 μm membranes.

5.2.3. Electro spraying of ZnO Nanorods onto PVDF Nanofiber Mat

In this study, 10 mL of 1.5 wt% ZnO nanorods in water was sonicated for 90 min and then electro sprayed onto PVDF nanofiber mats on the collector. The flow rate was 10 mL/h, and the rest of the parameters were the same as the electrospinning process for PVDF.

5.2.4. Hydrothermal Growth of ZnO Nanorods

Previously, we have demonstrated the successful growth of ZnO on a PVDF nanofiber surface.⁵⁹ The hydrothermal growth method of ZnO nanorods on PVDF nanofiber was modified from a similar growth method on cotton or nylon microfibers.^{30,54–56} First, solution concentration was diluted more than those in previously reported methods, thus resulting in smaller nanorods that would be in the range of nanofiber diameter. Second, the seeding step was repeated three times to produce nucleation sites on a more chemically inert PVDF fiber surface than nylon or cotton.⁵⁶ Third, the reaction

temperature was lowered to 60°C to prevent the heat relaxation of semi-crystalline PVDF nanofibers.⁵⁷ Finally, equimolar amounts of hexamethylenetetramine and zinc nitrate hexahydrate in the growth solution were replaced by a higher concentration of hexamethylenetetramine to yield the preferred ratio of the length to diameter of ZnO crystals.^{55,58}

ZnO Seed Solution

The seed solution was prepared in 50 mM concentration and diluted to 10 mM before use. Zinc acetate dihydrate ($\text{Zn}(\text{Ac})_2 \cdot 2\text{H}_2\text{O}$, 1.6462 g) was dissolved in 150 mL of isopropyl alcohol at 85°C with a vigorous stir at 1,000 rpm for 17 min. Triethylamine ($\text{N}(\text{CH}_2\text{CH}_3)_3$, 0.7637 g) was added dropwise to the solution and stirred again at 85°C, 400rpm for 13 min. The resulting 50 mM seed solution was incubated at room temperature without stirring for 6 h.⁵⁹

ZnO Growth Solution

The growth solution was prepared in 100 mM concentration and diluted to 10 mM before use. Hexamethylenetetramine ($\text{C}_6\text{H}_{12}\text{N}_4$, 9.3457 g) was dissolved in 400 mL of room-temperature deionized (DI) water, and the solution was stirred for 10 min. Zinc nitrate hexahydrate ($\text{Zn}(\text{NO}_3)_2$, 11.8991 g) was added to the solution and stirred for 24 h.⁵⁹

Growth of ZnO Nanorods on PVDF Fiber Surfaces

The successful growth of ZnO nanorods on cellulose or nylon fiber surfaces was achieved in previous work.^{17,30,54} Chemically, PVDF is more inert than cellulose or nylon, with more difficult seeding processes and fewer nucleation sites. During the seeding step of ZnO deposition, it is critical to form hexagonal nanorods arranged vertically to the substrate surface for the maximum strain rate transfer.⁵⁴ Therefore, the seeding process was repeated three times to provide sufficient nucleation sites.^{56,59} The oven temperature for seed curing and growth process was lowered to 60°C to inhibit the heat relaxation of PVDF and preserve the piezoelectric polarization of the electrospun fibers, thus avoiding an additional poling process.⁵⁷ Equimolar amounts hexamethylenetetramine and zinc nitrate hexahydrate in the growth solution were replaced by a higher concentration of hexamethylenetetramine to yield the preferred ratio of the polar and non-polar surface of ZnO crystals for higher piezoelectric responses.^{55,58}

5.2.5. Characterization

Field-emission scanning electron microscope (FESEM) images were taken using a Gemini 500 microscope (ZEISS, Oberkochen, Germany) with an accelerating voltage of 1 keV. To extract the detailed geometry with better focus and to reduce the charging effect under an FESEM, the samples were partially sputter coated with palladium/gold. The average PVDF fiber diameter and ZnO nanorod length and diameter were determined using FESEM images over 30 fibers with the ImageJ software (NIH, Bethesda, Rockville, MD, USA).⁴¹

Transmission electron microscope (TEM) images were taken using a T12 Spirit microscope (FEI, Lausanne, Switzerland) with an accelerating voltage of 120 keV. Nanofiber samples were placed between a copper oyster grid.

The crystallography of PVDF nanofibers and ZnO nanorods was examined by X-ray diffraction (XRD) with the theta-theta diffractometer (D8 GADDS, Bruker), and Cu- $K\alpha$ radiation ($= 1.54 \text{ \AA}$) at a 0.02° scanning step and an operating voltage of 40 kV and a current of 40 mA were used.

Fourier-transform infrared (FTIR) spectroscopy from $4,000$ to 650 cm^{-1} (Frontier FTIR, PerkinElmer, Waltham, MA, USA) was performed at room temperature to evaluate the polymer crystalline phase; FTIR spectra were collected with 16 scans and a resolution of 4 cm^{-1} .

Thermal gravimetric analyses (TGA) were used to determine the amount of ZnO added to PVDF nanofibers (Q500 Thermogravimetric Analyzer, TA Instruments, New Castle, DE, USA) by the heat removal of PVDF. Samples were heated up from room temperature to 990°C with the rate of $10^\circ\text{C}/\text{min}$ on a ceramic pan under a nitrogen ambient.

5.2.6. Piezoelectric Testing

The piezoelectric testing module was assembled by sandwiching the piezoelectric nanofiber mat between two electrodes made by conductive fabric (cotton and silver blend double jersey knit purchased from LessEMF, Latham, NY, USA). Wires were connected to the electrodes using conductive ink and epoxy.

The piezoelectric performance of the electrospun samples was evaluated by periodic tensile testing in a customized setup with a motorized actuator controlled by a controller and a module (ni-cRIO 9036 and ni-9503, National Instruments, Austin, TX, USA), a pressure sensor (LC201-300/N, Newport Electronics, Santa Ana, CA, USA), an electrometer (6517B, Keithley Instruments, Cleveland, OH, USA), a multimeter (34470A, Keysight, Santa Rosa, CA, USA), a source meter (2400, Keithley, Cleveland, OH, USA), and a programmable DC power supply (9130, BK Precision, Yorba Linda, CA, USA). The open-circuit voltage was measured with a Keithley 6517B electrometer, and the closed-circuit current was measured with a Keithley 2400 source meter. The testing head movement was set to 1 Hz, and the impact pressure was set to 0.10 MPa, which is within the human foot pressure range of 0–0.20 MPa,^{42–44}, although the applications are not limited to shoes. LabView software (National Instruments, Austin, TX, USA) was used to control all the components and to record voltage and current outputs synchronously.

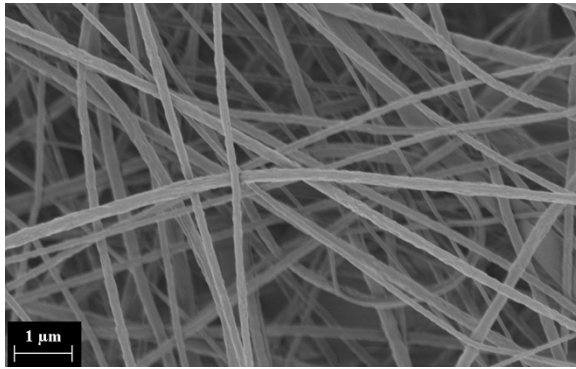
5.3. Results and Discussion

The effect of adding ZnO nanorods as fillers of PVDF nanofibers was investigated, such as morphology, PVDF β phase, and piezoelectricity.

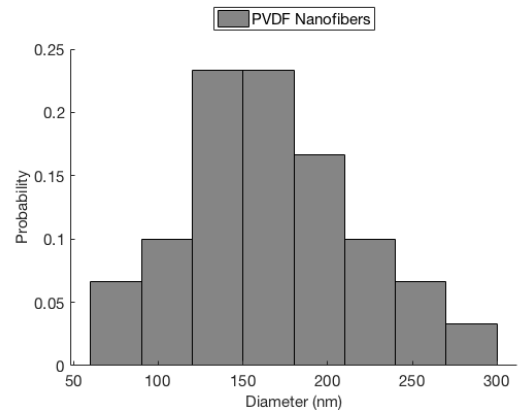
5.3.1. Material Analysis

The morphology of PVDF nanofibers and three composites—PVDF fibers with ZnO fillers (ZnO+PVDF), ZnO nanorods grown on the fiber surface (ZnO@PVDF), and

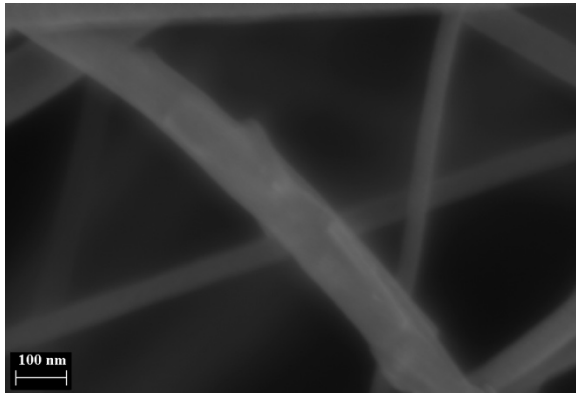
electrosprayed on the nanofiber mat surface (ZnO/PVDF)—were examined using an FESEM. Figure 17 illustrates the morphology, the size distribution of the PVDF nanofiber diameter, and the ZnO nanorod diameter and length.



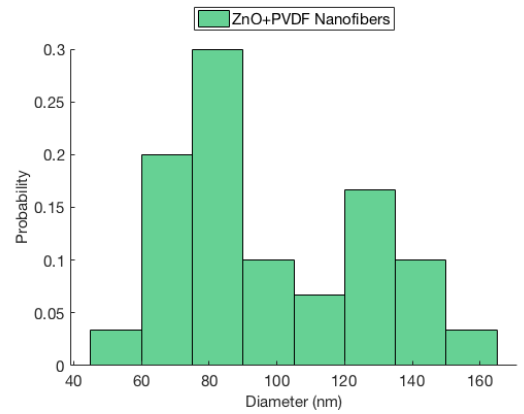
(a)



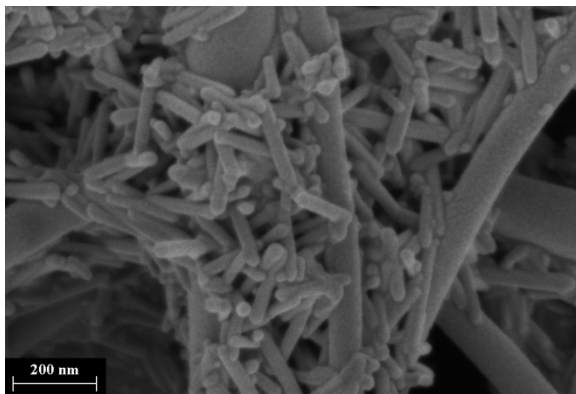
(b)



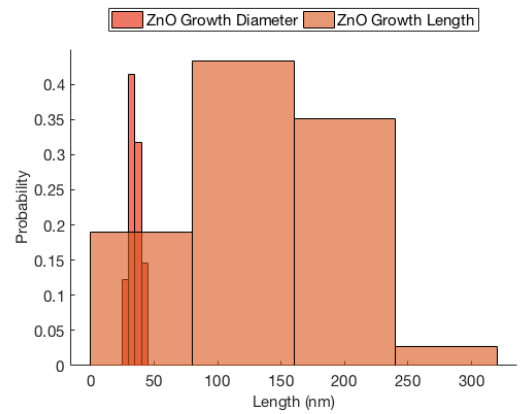
(c)



(d)



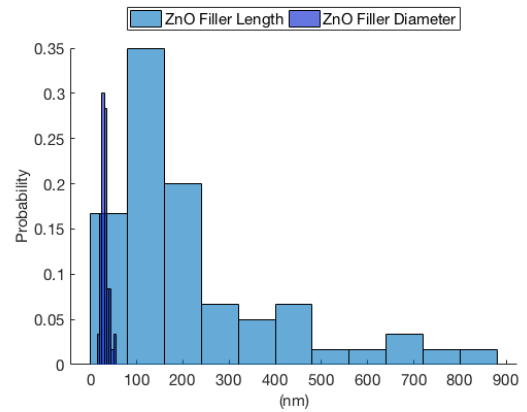
(e)



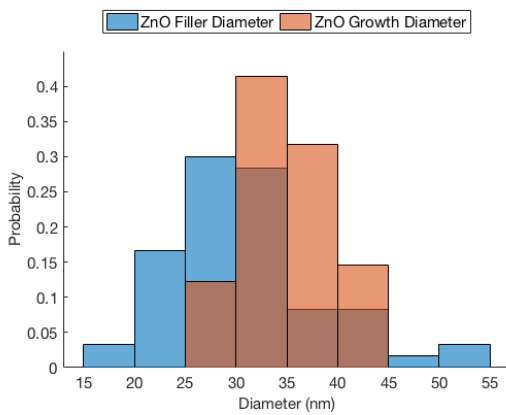
(f)



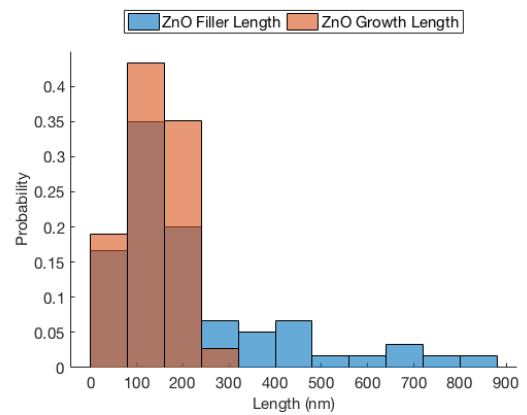
(g)



(h)



(i)



(j)

Figure 17. FESEM images of the (a) electrospun PVDF nanofibers; (c) ZnO nanorod fillers in PVDF nanofibers (ZnO+PVDF); (e) ZnO growth on a PVDF nanofiber surface (ZnO@PVDF); (g) ZnO nanorods electrospayed onto PVDF nanofiber mats (ZnO/PVDF). Nanofiber diameter analysis of electrospun (b) PVDF and (d) PVDF with ZnO fillers. Diameter and length analysis of (f) ZnO nanorods grown at 60°C; (h) ZnO nanorods synthesized at 150°C; (i) diameter comparison; and (j) length comparison of ZnO grown at 60°C and 150°C.

The different FTIR spectra were studied to analyze the PVDF crystalline phases with ZnO fillers after the ZnO hydrothermal growth process and ZnO electrospaying. Figure

18 compares the FTIR spectra of the electrospun PVDF nanofibers and three composites (i.e., ZnO+PVDF, ZnO@PVDF, and ZnO/PVDF). Each spectrum was normalized by a signal of an internal standard at 1,454 cm⁻¹ corresponding to the CH₂ in-plane bending.⁴⁵ All samples exhibit two strong polar β crystalline peaks at 840 cm⁻¹ (β , CH₂ rocking) and 1,276 cm⁻¹ (β , CF out-of-plane deformation), and weak, non-polar, α crystalline peaks at 614 cm⁻¹ (α , CF₂ bending and skeletal bending), 762 cm⁻¹ (α , CF₂ bending), 796 cm⁻¹ (α , CF₂ rocking), and 975 cm⁻¹ (α , CH out-of-plane deformation).^{46,47} The effects of fillers, hydrothermal growth, and electrospaying of ZnO nanorods on PVDF β crystals were considered by the intensity of the α and β crystalline peaks. None of the samples changed dramatically in terms of the intensity of the α and β crystalline peaks. Furthermore, the β -phase percentage can be quantified using the following equation:

$$F_{\beta} = \frac{X_{\beta}}{X_{\alpha} + X_{\beta}} = \frac{A_{\beta}}{(K_{\beta}/K_{\alpha})A_{\alpha} + A_{\beta}} \quad (7)$$

where F_{β} represents the PVDF β -phase percentage, A_{α} and A_{β} denote their absorption bands at 762 and 840 cm⁻¹, and K_{α} and K_{β} are the absorption coefficients at the respective wavenumbers, which are 6.1×10^4 and 7.7×10^4 cm²·mol⁻¹, respectively.⁴⁷⁻⁴⁹ The calculated β -phase percentage for the electrospun PVDF nanofibers was 83.7%, 78.2% for ZnO+PVDF, 80.1% for ZnO@PVDF, and 67.8% for ZnO/PVDF. Electrospaying ZnO nanorods had the greatest effect on the depolarization of PVDF β crystals, while fillers and surface growth did not show a significant difference. From the comparison of the FTIR spectra, it can be concluded that the electrospaying step depolarized the PVDF nanofibers the most, and the addition of ZnO fillers did the least.

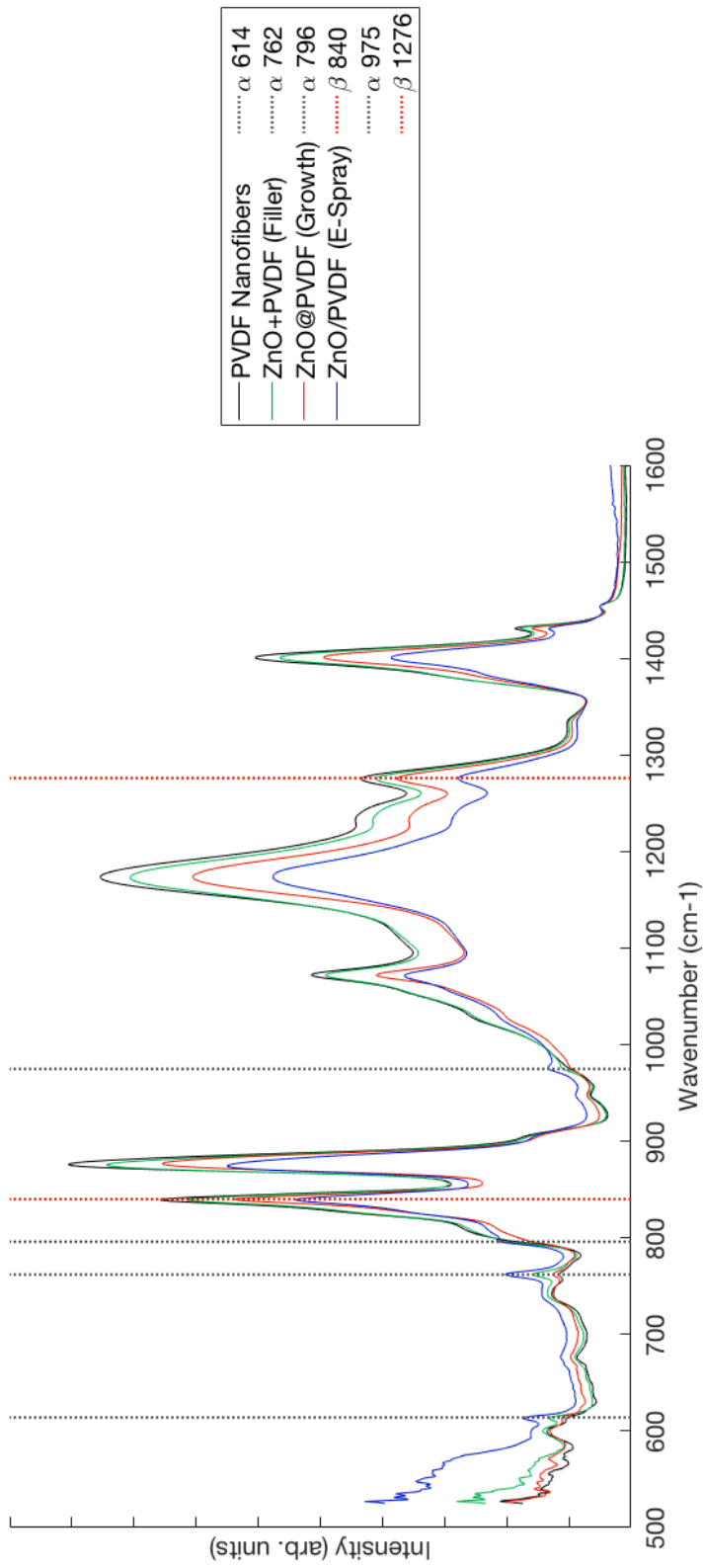


Figure 18. FTIR spectra showing the effect of the three ZnO nanorod addition methods to PVDF crystalline phases.

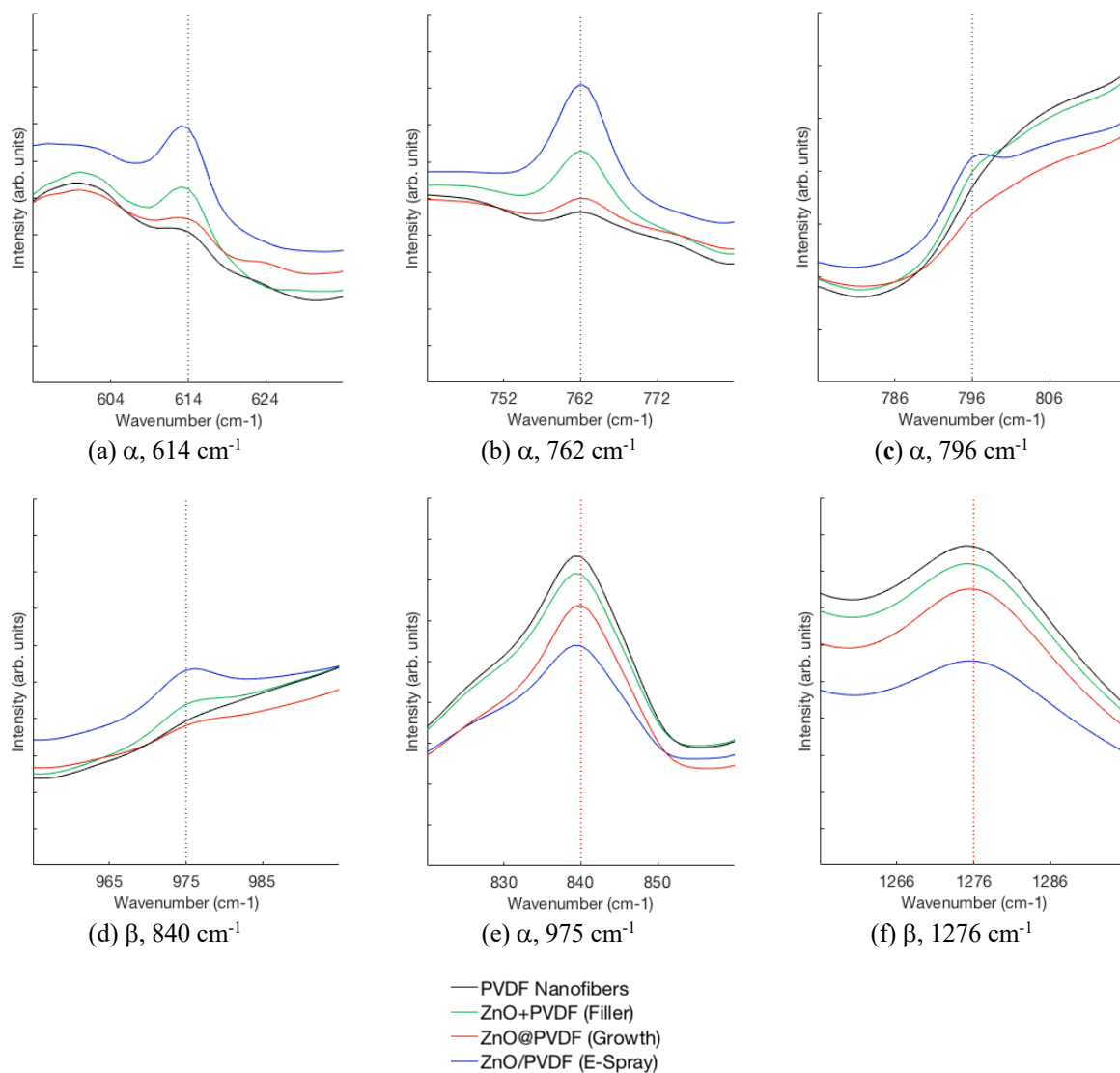


Figure 19. Peaks of FTIR spectra corresponding to α and β crystalline phases of PVDF: (a) α , 614 cm⁻¹; (b) α , 762 cm⁻¹; (c) α , 796 cm⁻¹; (d) β , 840 cm⁻¹; (e) α , 975 cm⁻¹; and (f) β , 1276 cm⁻¹.

The amount of ZnO added in the three composites was controlled to be close to 6 wt%. The weight percentage of ZnO in all composites was evaluated by TGA (Figure 20). The ZnO weight percentage of the ZnO+PVDF was 6.36 wt%, the ZnO@PVDF was 6.23 wt%, and the ZnO/PVDF was 6.20 wt%.

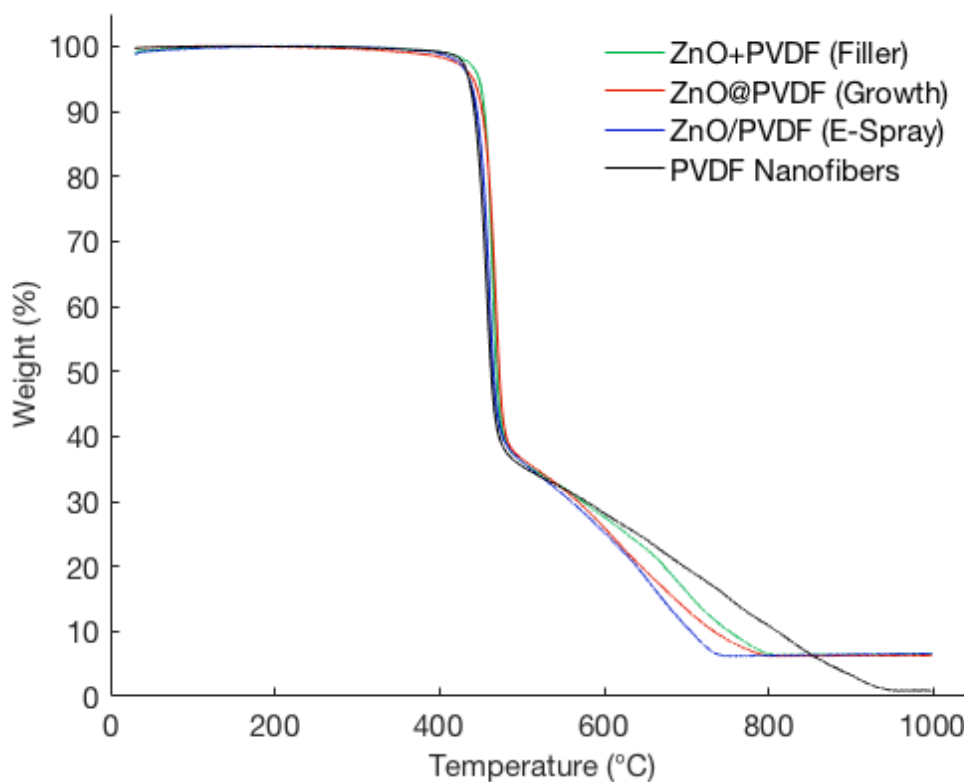


Figure 20. TGA of the PVDF membrane, ZnO+PVDF, ZnO@PVDF, and ZnO/PVDF.

Figure 21 displays the X-ray diffraction patterns of the electrospun PVDF nanofibers and three types of ZnO and PVDF composite nanofibers. The electrospun PVDF nanofibers exhibited strong peak 2θ values at 20.4° , which correspond to the β -phase

crystalline. Three ZnO and PVDF composite nanofibers have reflection peaks at 2θ values of 31.9° (100), 34.5° (002), 36.4° (101), 47.7° (102), 56.8° (110), 63.1° (103), and 66.7° (112), which can be indexed as the hexagonal wurtzite structure.^{50,51} No diffraction peaks from any other impurity phases were found, confirming that only single-phase hexagonal ZnO was present. Peaks corresponding to the (100), (002), (101), (102), (110), (103), and (112) planes of ZnO confirmed the successful incorporation of ZnO wurtzite crystals to the PVDF matrix.^{52,53} There was no significant difference in the PVDF α and β crystalline peak with the ZnO+PVDF and the ZnO@PVDF composite, whereas the ZnO/PVDF composite's β crystalline peak decreased slightly, which corresponds with the FTIR spectra results.

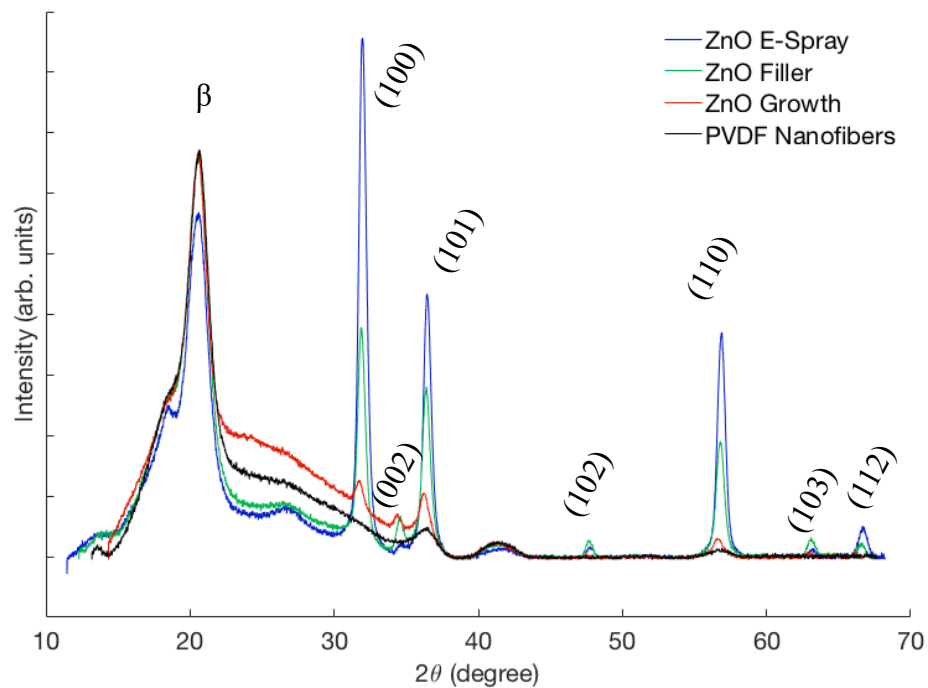


Figure 21. XRD spectra of the PVDF membrane and three types of ZnO and PVDF composites.

5.3.2. *Piezoelectric Measurements*

The piezoelectric testing module of PVDF and its composites was assembled by sandwiching the piezoelectric nanofiber mat between two electrodes made by conductive fabric.

The closed-circuit currents of the nanogenerators with different resistive loads were compared, and the closed-circuit voltages and the power density were derived accordingly. Table 4 lists the average values of the maximum peak currents with resistive loads of 0.47, 15, 30, and 60 M Ω . Figure 22a shows the nanogenerator load curve with all the data points from the different loads. Nonlinear least-square fitting was performed using the following equation:

$$V = V_{oc}(1 - \exp((I - I_{sc})/I_0)) \quad (8)$$

where V represents the measured voltage, I denotes the measured current, and V_{oc} , I_{sc} , and I_0 are the extracted parameters of the open-circuit voltage, short-circuit current, and I-V sharpness fitting, respectively. Figure 22b displays the typical transient current responses when the sample was subjected to cyclic compressive impacts with a resistive load of 15 M Ω .

As seen in Table 4 and Figure 22, the ZnO/PVDF nanogenerator produced the highest power output, with the ZnO@PVDF being the second highest; the ZnO+PVDF was lower than the as-spun PVDF. Among the three methods for adding ZnO nanorods to

PVDF, electrospaying increased the piezoelectric response the most, followed by hydrothermal growth; fillers had an adverse effect.

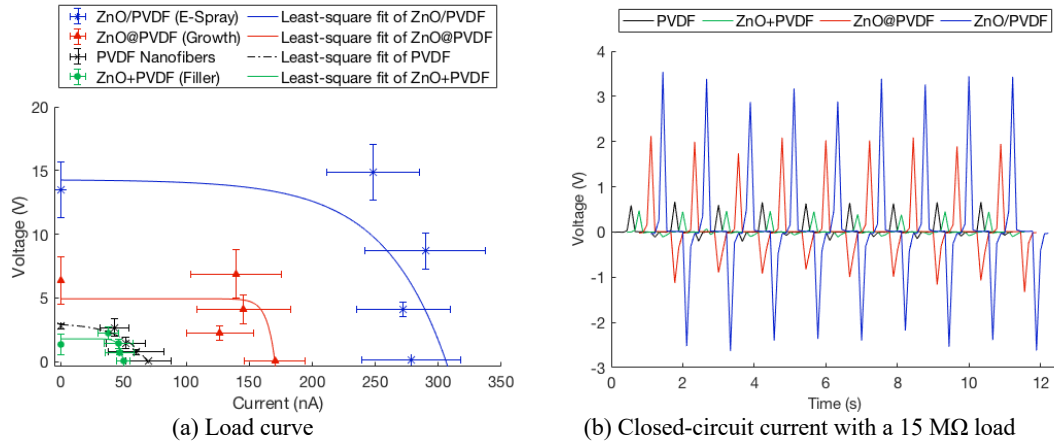


Figure 22. Nanogenerator characteristics of 15 cm² fiber mats: (a) load curves with resistive loads of 0.47, 15, 30, and 60 MΩ; and (b) transient closed-circuit current measurements with a 15 MΩ resistive load.

A possible explanation for the ZnO/PVDF having a higher piezoelectric response than the ZnO@PVDF could be the effect of the nanorod size difference. The findings indicate that ZnO nanorods synthesized at 150°C had a similar average diameter to the ZnO grown at 60°C, but the average length was 60% longer. As the ZnO nanorods used for the ZnO/PVDF and ZnO+PVDF were synthesized with the same recipe, the piezoelectric performance between the two composites could be the result of the PVDF acting as an insulator for the ZnO.

Table 4. Comparison of closed-circuit current and voltages of electrospun PVDF and three different types of ZnO and PVDF nanofiber composites.

		0.47 MΩ	15 MΩ	30 MΩ	60 MΩ
PVDF	Current (nA)	54.01	50.26	48.25	44.36
	Power Density (nW/cm ²)	0.09	2.53	4.66	7.87
	Voltage (V)	0.025	0.754	1.447	2.661
	Standard Deviation σ (V)	0.007	0.190	0.470	0.708
	Coefficient of Variation	0.29	0.25	0.32	0.27
ZnO@PVDF	Current (nA)	136.88	147.66	136.69	114.67
	Power Density (nW/cm ²)	0.59	31.80	37.37	52.60
	Voltage (V)	0.064	2.215	4.101	6.880
	Standard Deviation σ (V)	0.016	0.553	1.111	1.886
	Coefficient of Variation	0.25	0.25	0.27	0.27
ZnO/PVDF	Current (nA)	278.26	272.19	289.62	247.81
	Power Density (nW/cm ²)	2.43	74.09	167.76	245.63
	Voltage (V)	0.131	4.083	8.689	14.868
	Standard Deviation σ (V)	0.018	0.560	1.430	2.205
	Coefficient of Variation	0.14	0.14	0.16	0.15
ZnO+PVDF	Current (nA)	49.91	47.10	46.35	37.70
	Power Density (nW/cm ²)	0.08	2.22	4.30	5.69
	Voltage (V)	0.023	0.706	1.391	2.262
	Standard Deviation σ (V)	0.002	0.172	0.348	0.495
	Coefficient of Variation	0.10	0.24	0.25	0.22

5.3.3. Polarization Direction

A material analysis of the β -phase percentage of PVDF and ZnO peak intensity in relation to the piezoelectric response of three ZnO and PVDF composites revealed an inconsistency. In terms of piezoelectric response, the samples from highest to lowest were: ZnO/PVDF, ZnO@PVDF, as-electrospun PVDF, and ZnO+PVDF. The β -phase percentage of PVDF calculated from the FTIR of the samples ordered highest to lowest are as follows: as-spun PVDF, ZnO@PVDF, ZnO+PVDF, and ZnO/PVDF. The ZnO nanorod peak intensity measured from XRD from strongest to weakest, are as follows:

ZnO/PVDF, ZnO+PVDF, and ZnO@PVDF. The polarization direction of ZnO and PVDF was studied further to understand all the contributing factors to the piezoelectric response of PVDF and its composites.

The polarization direction of ZnO is determined by the growth pattern, which is along the c-axis. Wurtzite-structured ZnO has preferential growth along the c-axis direction to minimize the free energy of the entire reaction system. The high-energy polar surface is in the c-axis direction, and therefore the incoming precursor molecules tend to be absorbed on the polar surface of ZnO nanorods to minimize the surface energy.^{55,66,67}

Two factors contribute to the polarization direction of PVDF: the induced electric field during electrospinning and the mechanical drawing of fibers caused by the whipping instability of the polymer jet.^{12,68-70} When using a drum collector, the electric field induced to the polymer jet and the collected nanofiber mat are perpendicular to each other. For the polymer jet, the electric field is in the direction of the fiber axis, and for the nanofiber mat, it is in the direction of the thickness. The resultant induced dipole direction could be either—or a combination of both. Mandal et al. claimed that it is along the thickness of the mat based on a comparison of the open-circuit voltage of one layer of electrospun P(VDF-TrFE) and two layers stacked in different thickness directions.⁷¹ The voltage response of two layers stacked in the opposite direction decreased by approximately 75% in comparison to one layer. Tsai et al. proved that the resultant dipole direction is in the fiber axis by manipulating the electrospun PVDF yarn in the electric field. The yarn moved in the direction to align the yarn dipole direction and electric field direction.⁷² To define the dipole direction of our electrospun PVDF nanofiber mat, both Mandal and Tsai's methods were utilized.

First, the voltage response of the piezoelectric module with one layer of PVDF, and two layers of PVDF membranes staked in different polarization directions were compared according to the method proposed by Mandal et al. The average open-circuit voltage response of the single PVDF layer module was 2.37 V and 1.55 V for the double PVDF layers (Figure 23a). The decrease was 34%, much smaller than the 75% value from Mandal et al.; the dipole alignment of our PVDF mat in the thickness direction was present but not the dominant direction.

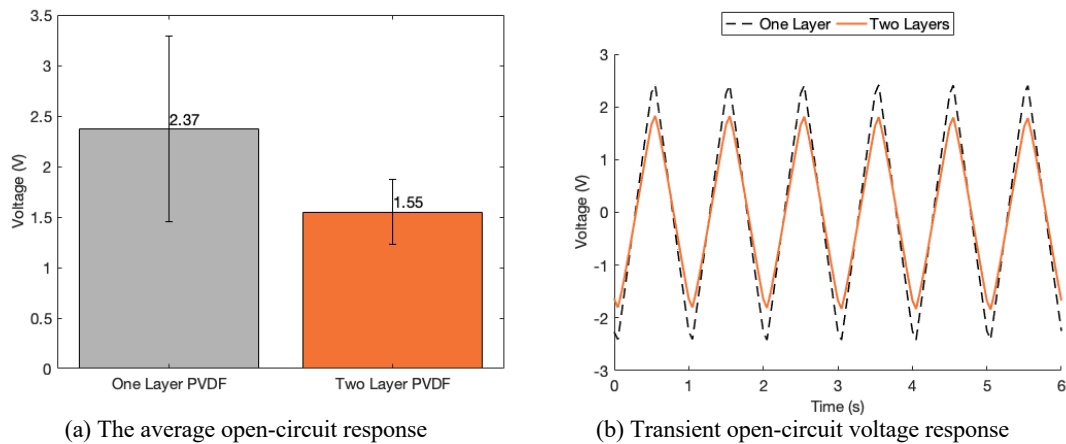


Figure 23. Polarization direction compression study in thickness direction: (a) the average open-circuit voltage response of one-layer PVDF and two layers stacked in the opposite thickness direction; and (b) transient open-circuit voltage measurements.

Second, the behavior of the electrospun nanofiber mats in a high electric field was observed, mirroring the work of Tsai et al. Electrospun PVDF mats were cut into rectangles where the length was aligned to the rotation of the drum collector (L_r , Figure

24a) or perpendicular to it (L_p , Figure 24b). Figure 25 describes how the samples were placed in the external electric field; the placement of the PVDF membrane was between the high-voltage clip and the grounded collector in the air. Two samples (L_r and L_p) were each tested using three alignments within the testing apparatus. The three alignments used for testing were a thickness-facing observer (L_{rt} and L_{pt}), a top-facing observer (L_{rf-t} and L_{pf-t}), and a bottom-facing observer (L_{rf-b} and L_{pf-b}), all with the electric field aligned with the membrane thickness or fiber-axis polarization direction. The top surface is the side facing the high-voltage clip during electrospinning, and the bottom is the side touching the ground collector. Figure 26 illustrates the results, and the green arrow indicates the thickness direction facing the observer, the red arrows indicate the drum-rotation direction, the solid red lines are for the top surface-facing observer, and the dashed red lines show the bottom surface-facing observer.

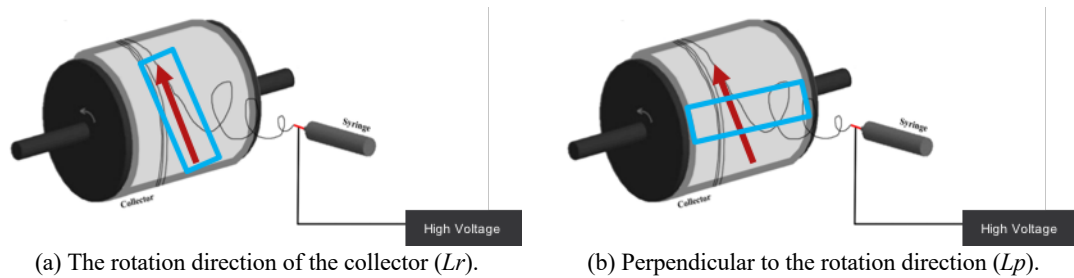


Figure 24. Electrospun PVDF membrane cut direction: (a) the rotation direction of the collecting drum (L_r); and (b) perpendicular to the drum-rotation direction (L_p).

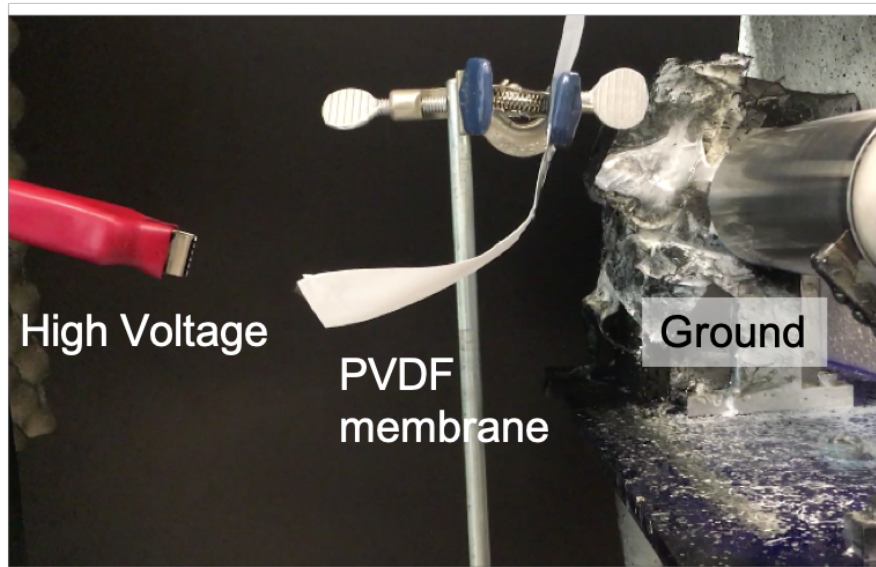


Figure 25. Testing setup for PVDF membrane behavior in the high electric field.

According to test results, the membranes with polarization direction and external electric field aligned to thickness direction (Lrt and Lpt) moved to be in alignment with the fiber axis around 14 kV. The samples aligned in the fiber-axis direction ($Lrf-t$, $Lpf-t$, $Lrf-b$, and $Lpf-b$) twisted in such a way as to orient the top surface of the mat to face upwards around 18 kV. Polarization in the fiber-axis direction was stronger than in the thickness direction, as indicated by the weaker external electric field required to move the mats in the thickness direction (Lrt and Lpt) compared to the mats in the fiber-axis direction ($Lrf-t$, $Lpf-t$, $Lrf-b$, and $Lpf-b$). Also, all samples moved to the fiber-axis direction. Polarization in the thickness direction was also present, as shown by the top surface of the mat reorienting to face upwards when the movements occurred.

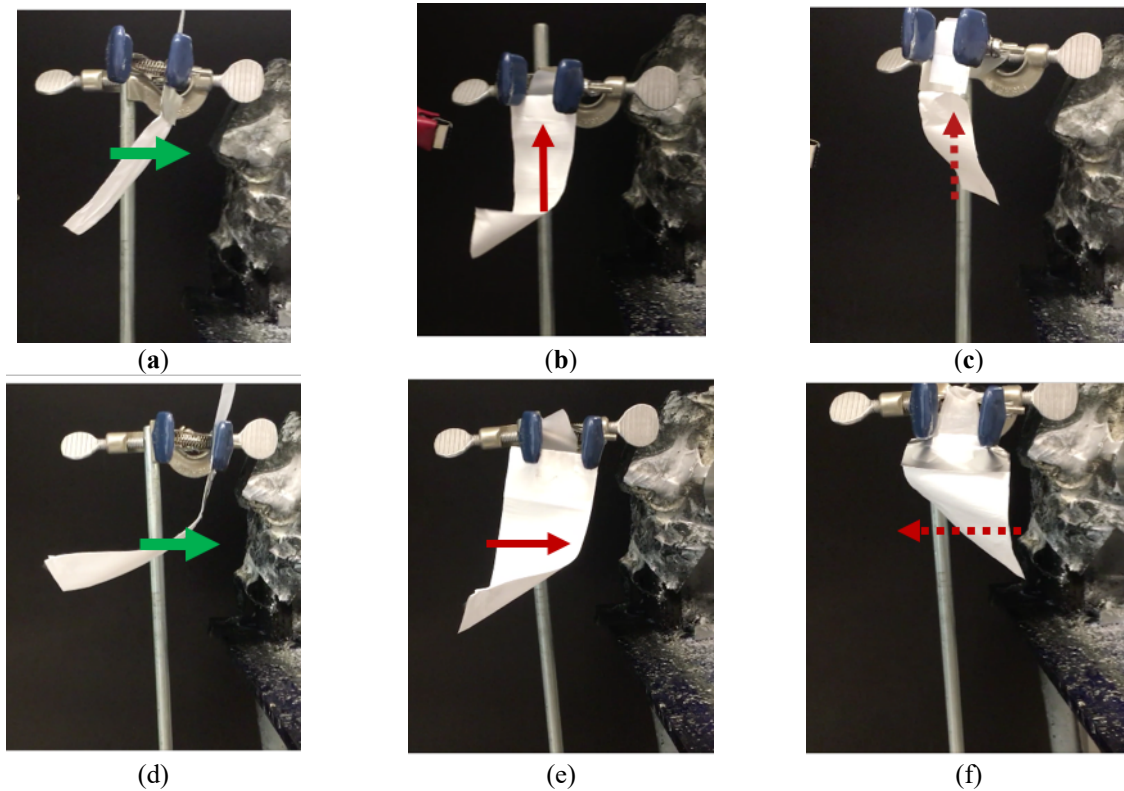


Figure 26. Green arrows indicate that the membrane thickness is facing the observer, as well as the direction of the thickness-polarization direction. Solid red arrows indicate the top surface-facing observer and the drum-rotation direction. Red arrows in dashes indicate the bottom-facing observer and the drum-rotation direction. (a) PVDF membrane rectangle length aligned to the drum-collector rotation direction and the membrane thickness-facing observer (Lrt); (b) Membrane rectangle length perpendicular to the collector rotation direction and the top surface-facing observer ($Lrf-t$); (c) Membrane rectangle length aligned to the collector rotation direction and the bottom surface-facing front ($Lrf-b$); (d) PVDF mat rectangle length perpendicular to the drum-collector rotation direction and the membrane thickness-facing observer (Lpt); (e) Membrane rectangle length perpendicular to the collector rotation direction and the top surface-facing front ($Lpf-t$); (f) Membrane rectangle length perpendicular to the collector rotation direction and the bottom surface-facing front ($Lpf-b$).

The resultant dipole direction of electrospun PVDF mat was a combination of the fiber-axis and mat-thickness direction, where the fiber-axis direction was the dominant one. The first study with the comparison of the voltage response of the piezoelectric module with one layer of PVDF, and two layers of PVDF membranes staked in different polarization directions revealed that the thickness-direction polarization contribution to the open-circuit voltage was 34%, meaning that it was present but not dominant. The second study, with the alignment of the mat in the high electric field, uncovered stronger polarization in the fiber-axis direction than in the mat-thickness direction, and the resultant polarization was the combination of the two.

5.4. Conclusions

Our nanogenerator performance was compared with those of the previous methods and presented in Table 5. While the open-circuit voltage of the breathable ZnO@PVDF and ZnO/PVDF fibrous nanogenerators exceeded the reported non-breathable fibrous nanogenerators with rigid plastic casings, the power generated was relatively lower due to the lower load of the current, probably due to imperfect contact between the fabric electrodes and the piezoelectric membrane. Having an external plastic casing can eliminate the airgap between electrodes and piezoelectric fibers, thus, ensure a seal between materials by applying constant stress. However, it makes the nanogenerator unbreathable and inflexible for wearable applications. Assembling the fibrous nanogenerators without using an impermeable and less flexible plastic casing while maintaining excellent contacts between the layers remains a challenge that should be further investigated for wearable applications of next-to-skin nanogenerators.

Table 5. Performance comparison of ZnO+PVDF, ZnO@PVDF, and ZnO/PVDF with conductive-knit electrodes to other works of flexible and breathable films.

	(units)	PVDF	ZnO+PVDF	ZnO@PVDF	ZnO/PVDF	Lee et al. ¹⁶	Zeng et al. ¹⁵	Fang et al. ¹⁷
Material		PVDF	PVDF, ZnO	PVDF, ZnO	PVDF, ZnO	PVDF, ZnO	PVDF, NaNbO ₃	PVDF
Fabrication method		Electrospinning	Electrospinning	Electrospinning	Electrospinning	Dip coating	Electrospinning	Needleless electrospinning
Ceramic addition		-	Filler	Growth	Electrospinning	Growth	Filler	-
Pressure or strain	(MPa or %)	0.1 MPa	0.1 MPa	0.1 MPa	0.1 MPa	< 1%	0.2 MPa	0.05 MPa
Frequency	(Hz)	1	1	1	1	~1	1	5
Open-circuit voltage	(V)	2.8	1.3	6.4	13.5	0.1	3.2	2.6
Closed-circuit current	(μ A)	0.05	0.05	0.15	0.30	-	4.2	4.5
Current density	(nA/cm ²)	3	3	9	19	10	672	2250
Current resistive load	(k Ω)	470	470	470	470	-	470	-

CHAPTER 6. BREATHABLE NANOGENERATORS

6.1. Introduction

Solid metals have excellent conductivity and are frequently used as electrodes. However, they are impermeable, which prevents the assembled material from being breathable or suitable for wearable purposes. This chapter features a comparison of aluminum foil as an example of solid metal and conductive-knit fabric as a breathable electrode material.

6.2. Materials and Methods

6.2.1. Electrode Materials

The piezoelectric testing module was assembled by sandwiching the piezoelectric nanofiber mat between two electrodes made by either conductive fabric (cotton and silver blend double jersey knit purchased from LessEMF, Latham, NY, USA) or aluminum foil. The average thicknesses of the aluminum foil and the conductive-knit electrode were 24.2 ± 5.8 , and 599 ± 14.3 μm , respectively. The sheet resistance of the conductive-knit and the aluminum foil were 1459 ± 6 and 413 Ω , respectively.

6.2.2. Breathability

The water-vapor permeability (WVP) was measured with an upright cup method according to British Standard specification for water vapour permeable apparel fabrics, BS 7209.^{73–75} The tests were conducted in a conditioned room with a temperature of $22.5^\circ\text{C} \pm 0.5^\circ\text{C}$ and relative humidity of $59.0\% \pm 1.5\%$. Samples were conditioned in the conditioning room over 24 h. The turntable holding cups were rotated uniformly to

avoid the formation of still air layers above the test dishes at 2.3 m/min. The aluminum cups used in this experiment had an inner diameter of 83 mm, an outer diameter of 90 mm, an inner cup thickness of 18.5 mm, and an outer cup thickness of 20 mm. Each cup contained 18 g of deionized (DI) water, and triangular support was used to prevent the samples from sagging into the cup. The samples were tested for over 60 h to determine the water mass loss over time due to the WVP of the test samples.

6.2.3. Piezoelectric Testing

Figure 27a displays a photo of the breathable fibrous nanogenerator, which consists of a piezoelectric nanofiber membrane sandwiched by two conductive-knit electrodes, and Figure 27b shows a non-breathable nanogenerator with aluminum foil. Wires were connected to the electrodes using conductive ink and epoxy.

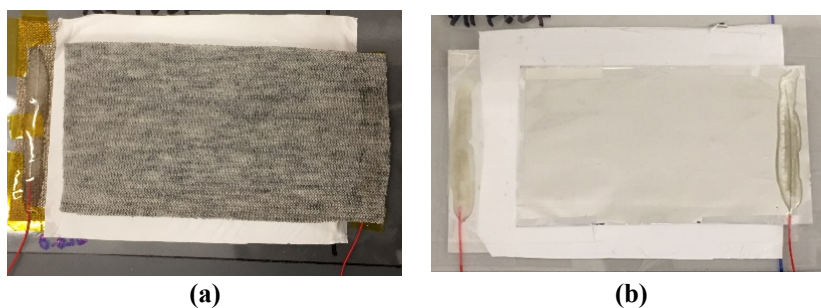


Figure 27. (a) The breathable fibrous nanogenerator with conductive knits and (b) the non-breathable nanogenerator with aluminum foil.

6.3. Results and Discussion

6.3.1. Mechanical Properties

Material Breathability

The breathability of piezoelectric fibrous nanogenerators, as well as that of the constituent materials, was evaluated by measuring the WVP of the nanogenerators, which consisted of an electrospun PVDF membrane sandwiched by two layers of conductive-knit. An upright cup method was employed using the BS 7209 standard.^{74,75} A woven cotton fabric was also tested at the same time for a benchmark. The WVP was calculated using the following formula:

$$\text{WVP} = \frac{24 M}{At} \quad (9)$$

where WVP is the rate of water-vapor permeability ($\text{g} \cdot \text{m}^{-2} \cdot \text{day}^{-1}$), M represents the loss in mass (g), t denotes the time duration (h), and A is the area of the exposed test fabric, which is equal to the internal area of the dish (m^2). The results were averaged from three specimens for over 60 h.

As demonstrated in Table 6, all the materials used in the nanogenerator had similar WVP, which is also comparable to that of the woven cotton fabric. The electrospun PVDF membrane's WVP decreased slightly after ZnO growth on the surface, but the difference was small. The fact that the nanofibrous materials studied had smaller WVP than microscale fabrics did aligns with other works in this field related to theory and experiments on the gas diffusion behavior of nanoscale and microscale fibrous media.^{76,77} The conductive-knit was more breathable than the electrospun membranes or woven cotton. The three-layer nanogenerator assembly with PVDF had the lowest WVP. However, it is interesting to see that the resulting WVP was not reduced proportionally to the stack of the individual layers but only slightly less than each layer. The fact that the nanogenerator assembly WVP was not proportional to the number of layers may stem from the conductive-knit's much larger pores and the still air layer

associated with the nanogenerator assembly, which is not much different from that on the single layer.

Table 6. Water-vapor permeability (WVP) for various membranes and fabrics.

WVP (g·m ⁻² ·day ⁻¹)	PVDF	ZnO@PVDF	Conductive knit	Nanogenerator assembly by PVDF	Cotton
Average	629.00	623.68	645.57	608.20	611.82
Standard Deviation σ	31.95	16.92	26.98	15.05	32.02
Coefficient of Variation	0.05	0.03	0.04	0.03	0.05

6.3.2. Piezoelectric Measurement Comparison of Aluminum Foil and Conductive-Knit Fabric as Electrodes

Aluminum foil and conductive-knits were used as electrodes for comparison. Four types of nanogenerators were made with two types of piezoelectric nanofibrous membranes (i.e., PVDF and ZnO@PVDF) and two types of electrodes (i.e., aluminum foil and conductive-knits). Open-circuit voltages were measured to evaluate the two electrode materials. Figure 28 shows the cyclic responses of the piezoelectric nanogenerators when the module was subjected to repeated compressive impacts. The average values, standard deviation, and coefficient of variation of the maximum open-circuit voltage when the piezoelectric nanogenerators were subjected to repeated compressive impacts are listed in Table 7. A custom-made cyclic compression tester was used to impact the nanogenerator with an effective area of 15 cm², a frequency of 1 Hz, and a pressure of 0.10 MPa, emulating foot pressure during walking.

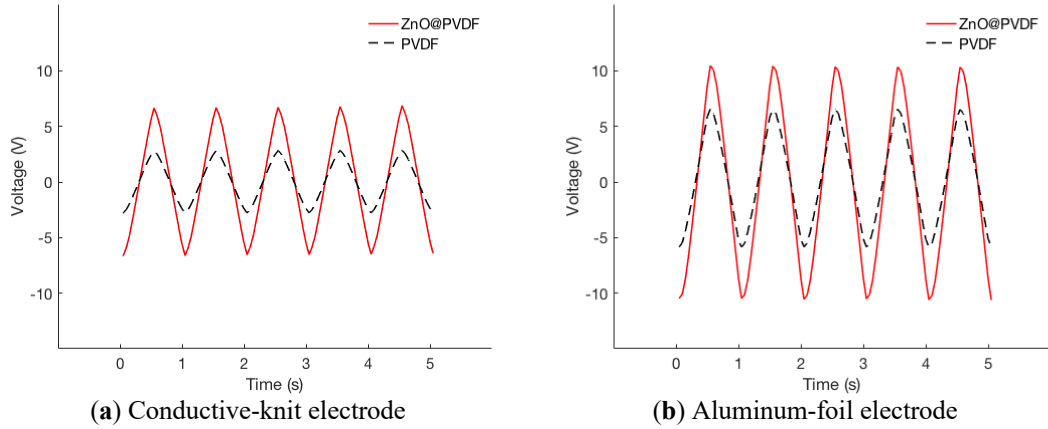


Figure 28. Open-circuit voltage measurements under a 0.10 MPa impact of 1 Hz frequency: (a) a conductive-knit electrode nanogenerator and an (b) aluminum-foil electrode nanogenerator. The black lines in dashes represent PVDF, while the red lines stand for ZnO@PVDF.

Table 7. Open-circuit voltages for piezoelectric samples under a 0.10 MPa impact of 1 Hz frequency.

Materials	Conductive-knit electrode			Aluminum-foil electrode		
	Average (V)	Standard deviation σ (V)	Coefficient of variation	Average (V)	Standard deviation σ (V)	Coefficient of variation
PVDF	2.76	0.22	0.08	6.26	3.51	0.56
ZnO @PVDF	6.36	1.89	0.30	10.84	6.12	0.56

Open-circuit voltages for aluminum-foil electrodes were found to be higher than those for conductive-knit electrodes for both PVDF and ZnO@PVDF. Also, the variation of measurements was more significant for aluminum foil than for the conductive-knits. A possible explanation for the more stable and reproducible results of the conductive-knit electrodes is that they provided better adherence between the piezoelectric membrane and the electrodes. We opted not to use any additional casing to press the adhesion of electrodes and piezoelectric membrane layers to maintain the best flexibility and

breathability, and thus the air gap between the layers could exist due to the lack of external forces. The flexibility and stretchable quality of the materials determine the size of the air gap created. Such properties can be measured with the Fabric Assurance by Simple Testing (FAST) system.⁷⁸ The bending and shear rigidity of the conductive-knits were $0.87 \pm 0.05 \mu\text{N}\cdot\text{m}$ and 21.42 N/m , respectively. For aluminum foil, the values were beyond the measurement range of the FAST system. The aluminum-foil electrodes have higher absolute piezoelectric measurements since the aluminum sheets are more conductive than porous fabric. The open-circuit voltage of the nanogenerators used in this research, which is less affected by the existence of an air gap than by the load current, was significantly higher than those reported in the literature.¹⁵⁻¹⁷

6.4. Conclusions

High piezoelectric response, breathability, and flexibility are essential to nanogenerators for wearable applications. This study demonstrated that breathability and flexibility of the fibrous nanogenerators could be achieved by assembling a layer of an electrospun piezoelectric nanofibrous membrane with two layers of conductive-knit and without the use of rigid plastic casings.

CHAPTER 7. COMPARISON OF CONDUCTIVE KNITS AND METAL SHEETS AS ELECTRODES

7.1. Introduction

In Chapter 5, the comparison of our piezoelectric composite nanofibers' performance compared to those used in previous works demonstrated that ours had a magnitude higher in terms of open-circuit voltage response, while the current response was a magnitude smaller (Table 5). For this chapter, conductive fabric and aluminum sheets were used as electrode materials and compared to further study the effect of air gaps on high open-circuit voltage and the low-current response of our PVDF nanogenerators.

7.2. Materials and Methods

7.2.1. Electrode Materials

Conductive knits and aluminum sheets—599 μm and 3 mm in thickness, respectively—were used as electrodes. The piezoelectric testing module was assembled by sandwiching the piezoelectric nanofiber mat between two electrodes. As conductive knits are flexible and light, they create small air gaps between electrodes and the PVDF membranes. Solid and heavy 3 mm aluminum sheets were used to eliminate this air gap. Conductive silver paint and epoxy were used to attach wires to knits, and lead soldering was employed for aluminum.

7.2.2. Piezoelectric Testing

Figure 29 displays photos of the nanogenerator with conductive knits (a) and with aluminum sheets (b).

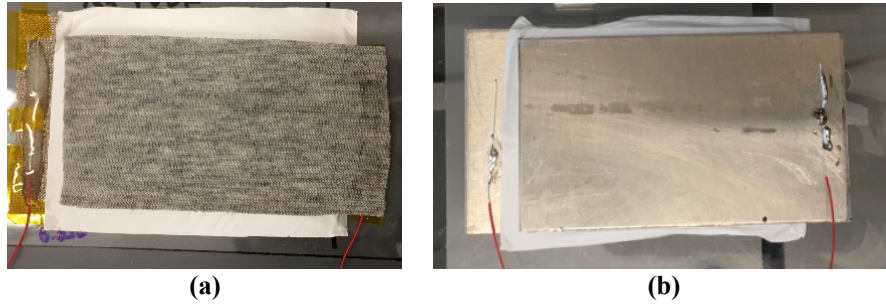


Figure 29. (a) The flexible fibrous nanogenerator with conductive-knit electrodes and (b) the solid nanogenerator with aluminum-sheet electrodes.

7.3. Results and Discussion

Open-circuit voltage and currents with a 470 k Ω load were collected to find the effect of the air gap between electrodes and piezoelectric nanofibers. Figure 30 shows the cyclic responses of the piezoelectric nanogenerators when the module was subjected to repeated compressive impacts. The maximum open-circuit voltage and closed-circuit current when the piezoelectric nanogenerators were subjected to repeated compressive impacts are listed in Table 8. A custom-made cyclic compression tester was used to impact the nanogenerator with an effective area of 15 cm², a frequency of 1 Hz, and a pressure of 0.10 MPa, emulating foot pressure during walking.

7.3.1. Open-circuit Voltage

Open-circuit voltage responses with conductive knits and aluminum sheets are graphed in Figure 30, and the decrease of the voltage response over time with the aluminum sheets is noticeable in Figure 30a. This result is suspected to be the effect of

the heavy aluminum sheet inhibiting the PVDF nanofiber mat's full recovery in thickness after repeated compressions.

The maximum open-circuit voltage response of the aluminum sheet was smaller than that of the conductive-knit electrodes. An additional triboelectric effect could explain this, of which created from the air gap. The triboelectric effect creates polarized charges from the contact electrification and electrostatic phenomena of two different materials.^{79,80} Airgap distance, surface roughness, materials, and so forth contributes to the triboelectric effect; in this experiment, airgaps between conductive-knit electrodes and the PVDF nanofiber mat created additional triboelectricity and resulted in a higher response than a mere piezoelectric response from aluminum-sheet electrodes.

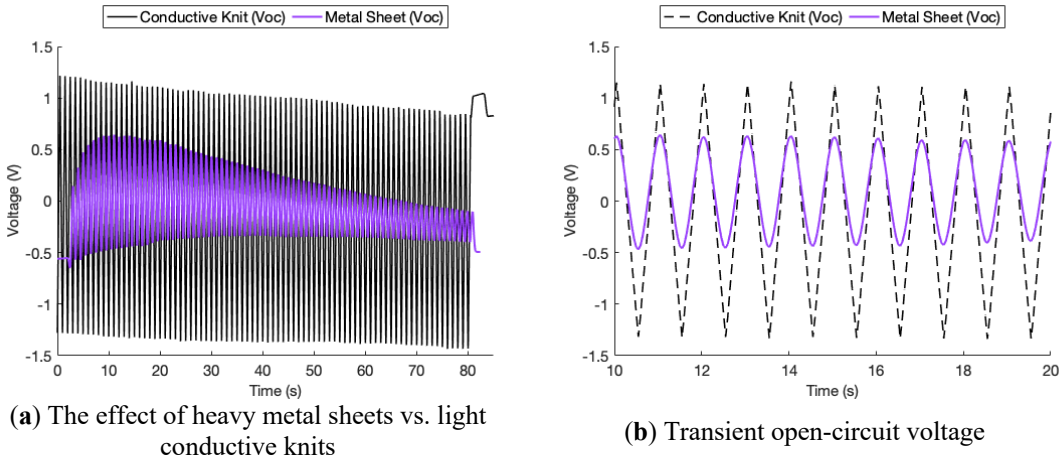


Figure 30. Transient open-circuit voltage measurements under 0.10 MPa impacts of 1 Hz frequency: (a) the effect of aluminum sheets' weight-restricting membrane thickness on recovery from compression over a long period of time and (b) enlarged responses over a short time. The black lines represent conductive-knit electrodes, and purple lines denote aluminum-sheet electrodes.

The high-voltage and low-current responses are a reported characteristic of triboelectric nanogenerators, and generally, they have higher output power than piezoelectric nanogenerators.^{6,79,81} Our nanogenerator also exhibited high-voltage and low-current responses, which aligns with these previous findings.

The triboelectric effect would also explain the higher piezoelectric response of the ZnO/PVDF and ZnO@PVDF compared to as-spun PVDF or ZnO+PVDF by increased surface roughness and the greater friction created, which is an important factor in improving triboelectric response.^{6,82,83}

Between ZnO/PVDF and ZnO@PVDF, the electrospaying method (ZnO/PVDF) resulted in higher power output. One of the possible explanations is that the electrospayed ZnO nanorods were not firmly attached to the PVDF compared to the grown ones (ZnO@PVDF) and that additional small movements of ZnO created the additional triboelectric effect.

7.3.2. Current with a Resistive Load

Current responses with a 470 k Ω resistive load of the conductive-knit and aluminum-sheet electrodes are displayed in Figure 31. The aluminum sheets had a significantly lower current response compared to the conductive knits. As explained by the open-circuit voltage response, this seems to be the combination of the low piezoelectric response of heavy aluminum sheets restricting membrane thickness recovery and the additional triboelectric effect with conductive knits.

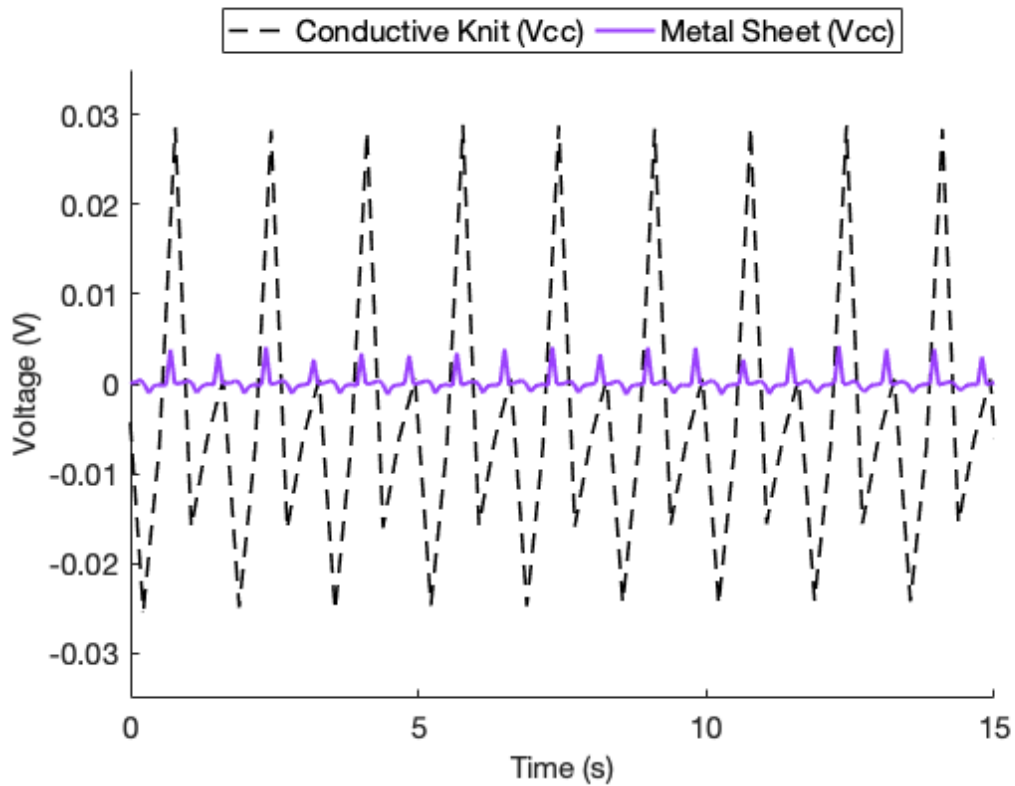


Figure 31. The transient closed-circuit current of the conductive-knit (black dash) and aluminum-sheet (purple line) electrodes with a 470 k Ω resistive load under a 0.10 MPa impact of 1 Hz frequency.

Table 8. Open-circuit voltages (Voc) and a closed-circuit current with a 470 k Ω resistive load (Vcc) comparison for conductive-knit and aluminum-sheet electrodes under a 0.10 MPa impact of 1 Hz frequency.

Materials	Conductive-knit electrode			Aluminum-sheet electrode		
	Average (V)	Standard deviation σ (V)	Coefficient of variation	Average (V)	Standard deviation σ (V)	Coefficient of variation
Voc	2.65	0.40	0.15	0.65	0.27	0.42
Vcc	0.032	0.016	0.51	0.002	0.002	0.86

7.4. Conclusions

The effects of air gaps between PVDF nanofibers and electrodes were studied by the comparison of conductive-knit and aluminum-sheet electrodes. Aluminum sheets had lower open-circuit voltage and closed-circuit currents than conductive knits. This was due to the lower piezoelectric response with heavy aluminum sheets inhibiting membranes' mechanical recovery from compressions and the lack of an additional triboelectric effect from the air gap. Increased contact due to the elimination of air gaps was not observed.

CHAPTER 8. CONCLUSIONS AND FUTURE WORKS

8.1. Conclusions

Electrospun PVDF and three composites with ZnO nanorods were explored as wearable nanogenerator materials. Electrospaying ZnO on PVDF (ZnO/PVDF) resulted in the highest power output, followed by ZnO growth (ZnO@PVDF), as-electrospun PVDF, and ZnO fillers (ZnO+PVDF). In addition, ZnO nanorods had an increased power output when they were on the PVDF surface due to the increased surface roughness of membranes, which contributed to a higher triboelectric response. When ZnO was embedded within the PVDF nanofiber, it made the materials more dielectric and resulted in lower power output.

Aluminum foil, conductive knits, and aluminum sheets were used as electrodes, allowing the breathability of conductive knits and the assembly with the PVDF membrane to be tested. Aluminum foil is a thin, light, and an easily accessible conductive material that was first explored as an electrode. This material showed variation in repeated compression testing results since the material became thinner and the air gap therefore increased. Conductive knit was introduced as a breathable and flexible conductive material with less variation in compression testing results; however, this material had more power output intensity due to its lower conductivity compared to solid metals. Finally, aluminum sheets were used to eliminate the air gap between PVDF membranes and electrodes, which were present in the modules with foils and knits. Despite the improved contact, the power output was lower and suggested that the triboelectric effect stemmed from air gaps in the modules with foils and knits.

8.2. Recommendations for Future Research

For ZnO hydrothermal growth on PVDF, achieving homogeneous growth of ZnO nanorods at low temperatures was not possible. Electrospinning ZnO cannot produce a strong link between ZnO and PVDF. Two methods could result in homogeneous samples with ZnO attached on the fiber surface. The first one involves using additional poling of PVDF after a ZnO growth temperature 80°C or higher. At high temperatures, ZnO nanorod growth would be homogeneous but would depole PVDF fibers, which would require an additional step of poling. The second method consists of coaxial spinning PVDF as a core and water-soluble polymer and ZnO nanorods as a sheath. Removing the sheath polymer after spinning would result in the alignment of ZnO nanorod axis with the PVDF fiber axis, and ZnO nanorods attached on the PVDF fiber surface. This method anticipates similar morphologies with a better attachment of ZnO to the PVDF fibers is anticipated. The effect of different morphologies, homogeneous ZnO distributions, and ZnO yield percentages after the sheath polymer removal on power output could be explored.

When it comes to wearables, breathability and flexibility are important for comfort. Fusing materials or external casings should not be used since doing so makes nanogenerators non-breathable and rigid. Our nanogenerators—without any fusing or external casings—exhibited a triboelectric and piezoelectric response to cyclic compressions. Further studies regarding bending, abrasion, or shear in human–clothing interaction could be investigated for the optimal power output and applications of wearable nanogenerators.

Conductive-knit electrode edges were not fixed, and the air gap between electrodes and the PVDF membrane created the triboelectric effect. In addition to comparisons between the aluminum-sheet electrodes, further study of assembly methods could be beneficial, such as the dotted glue technique used in Gore-Tex® that makes contact between materials more stable and creates less abrasion. Better contacts have the potential to increase the current output and reduce abrasion. Assembly would be mechanically more stable for durability while using or washing the materials.

A garment design study of prototype garments using the materials to find what parts of the body have the most potential for energy harvesting in piezoelectricity or triboelectricity or both could be studied. Diverse mechanical inputs, such as compression, bending, stretching, abrasion, and so forth, happen in human–clothing interactions, and these inputs also vary by the garment type or design, which would be beneficial information for researchers wishing to gain insights into product development.

REFERENCES

- (1) Anton, S. R.; Sodano, H. A. A Review of Power Harvesting Using Piezoelectric Materials (2003–2006). *Smart Mater. Struct.* **2007**, *16* (3), R1. <https://doi.org/10.1088/0964-1726/16/3/R01>.
- (2) Hu, Y.; Wang, Z. L. Recent Progress in Piezoelectric Nanogenerators as a Sustainable Power Source in Self-Powered Systems and Active Sensors. *Nano Energy* **2015**, *14*, 3–14. <https://doi.org/10.1016/j.nanoen.2014.11.038>.
- (3) Tao, X. *Smart Fibres, Fabrics and Clothing: Fundamentals and Applications*; Elsevier, 2001.
- (4) Zeng, W.; Shu, L.; Li, Q.; Chen, S.; Wang, F.; Tao, X.-M. Fiber-Based Wearable Electronics: A Review of Materials, Fabrication, Devices, and Applications. *Adv. Mater.* **2014**, *26* (31), 5310–5336. <https://doi.org/10.1002/adma.201400633>.
- (5) Zhang, M.; Gao, T.; Wang, J.; Liao, J.; Qiu, Y.; Yang, Q.; Xue, H.; Shi, Z.; Zhao, Y.; Xiong, Z.; et al. A Hybrid Fibers Based Wearable Fabric Piezoelectric Nanogenerator for Energy Harvesting Application. *Nano Energy* **2015**, *13* (Supplement C), 298–305. <https://doi.org/10.1016/j.nanoen.2015.02.034>.
- (6) Huang, T.; Wang, C.; Yu, H.; Wang, H.; Zhang, Q.; Zhu, M. Human Walking-Driven Wearable All-Fiber Triboelectric Nanogenerator Containing Electrospun Polyvinylidene Fluoride Piezoelectric Nanofibers. *Nano Energy* **2015**, *14* (Supplement C), 226–235. <https://doi.org/10.1016/j.nanoen.2015.01.038>.
- (7) Stoppa, M.; Chiolerio, A. Wearable Electronics and Smart Textiles: A Critical Review. *Sensors* **2014**, *14* (7), 11957–11992. <https://doi.org/10.3390/s140711957>.
- (8) Lovinger, A. J. Ferroelectric Polymers. *Science* **1983**, *220* (4602), 1115–1121. <https://doi.org/10.1126/science.220.4602.1115>.
- (9) Wang, X.; Shi, J. Piezoelectric Nanogenerators for Self-Powered Nanodevices. In *Piezoelectric Nanomaterials for Biomedical Applications*; Nanomedicine and Nanotoxicology; Springer, Berlin, Heidelberg, 2012; pp 135–172. https://doi.org/10.1007/978-3-642-28044-3_5.
- (10) Kochervinskii, V. V.; Kozlova, N. V.; Khnykov, A. Y.; Shcherbina, M. A.; Sulyanov, S. N.; Dembo, K. A. Features of Structure Formation and Electrophysical Properties of Poly(Vinylidene Fluoride) Crystalline Ferroelectric Polymers. *J. Appl. Polym. Sci.* **2010**, *116* (2), 695–707. <https://doi.org/10.1002/app.31044>.
- (11) Tichý*, P. J.; Erhart, D. J.; Kittinger*, P. D. E.; Přivratská, P. J. Piezoelectric Materials. In *Fundamentals of Piezoelectric Sensorics*; Springer Berlin Heidelberg, 2010; pp 119–185. https://doi.org/10.1007/978-3-540-68427-5_7.
- (12) Harrison, J. S.; Ounaies, Z. Piezoelectric Polymers. In *Encyclopedia of Polymer Science and Technology*; John Wiley & Sons, Inc., 2002. <https://doi.org/10.1002/0471440264.pst427>.

- (13) Kang, H. B.; Han, C. S.; Pyun, J. C.; Ryu, W. H.; Kang, C.-Y.; Cho, Y. S. (Na,K)NbO₃ Nanoparticle-Embedded Piezoelectric Nanofiber Composites for Flexible Nanogenerators. *Compos. Sci. Technol.* **2015**, *111* (Supplement C), 1–8. <https://doi.org/10.1016/j.compscitech.2015.02.015>.
- (14) Nunes-Pereira, J.; Sencadas, V.; Correia, V.; Rocha, J. G.; Lanceros-Méndez, S. Energy Harvesting Performance of Piezoelectric Electrospun Polymer Fibers and Polymer/Ceramic Composites. *Sens. Actuators Phys.* **2013**, *196* (Supplement C), 55–62. <https://doi.org/10.1016/j.sna.2013.03.023>.
- (15) Zeng, W.; Tao, X.-M.; Chen, S.; Shang, S.; Chan, H. L. W.; Choy, S. H. Highly Durable All-Fiber Nanogenerator for Mechanical Energy Harvesting. *Energy Environ. Sci.* **2013**, *6* (9), 2631–2638. <https://doi.org/10.1039/C3EE41063C>.
- (16) Lee, M.; Chen, C.-Y.; Wang, S.; Cha, S. N.; Park, Y. J.; Kim, J. M.; Chou, L.-J.; Wang, Z. L. A Hybrid Piezoelectric Structure for Wearable Nanogenerators. *Adv. Mater.* **2012**, *24* (13), 1759–1764. <https://doi.org/10.1002/adma.201200150>.
- (17) Fang, J.; Niu, H.; Wang, H.; Wang, X.; Lin, T. Enhanced Mechanical Energy Harvesting Using Needleless Electrospun Poly(Vinylidene Fluoride) Nanofibre Webs. *Energy Environ. Sci.* **2013**, *6* (7), 2196–2202. <https://doi.org/10.1039/C3EE24230G>.
- (18) Chang, J.; Dommer, M.; Chang, C.; Lin, L. Piezoelectric Nanofibers for Energy Scavenging Applications. *Nano Energy* **2012**, *1* (3), 356–371. <https://doi.org/10.1016/j.nanoen.2012.02.003>.
- (19) Bafqi, M. S. S.; Bagherzadeh, R.; Latifi, M. Fabrication of Composite PVDF-ZnO Nanofiber Mats by Electrospinning for Energy Scavenging Application with Enhanced Efficiency. *J. Polym. Res.* **2015**, *22* (7), 130. <https://doi.org/10.1007/s10965-015-0765-8>.
- (20) Shirinov, A. V.; Schomburg, W. K. Pressure Sensor from a PVDF Film. *Sens. Actuators Phys.* **2008**, *142* (1), 48–55. <https://doi.org/10.1016/j.sna.2007.04.002>.
- (21) Liu, F.; Hashim, N. A.; Liu, Y.; Abed, M. R. M.; Li, K. Progress in the Production and Modification of PVDF Membranes. *J. Membr. Sci.* **2011**, *375* (1), 1–27. <https://doi.org/10.1016/j.memsci.2011.03.014>.
- (22) Panda, P. K. Review: Environmental Friendly Lead-Free Piezoelectric Materials. *J. Mater. Sci.* **2009**, *44* (19), 5049–5062. <https://doi.org/10.1007/s10853-009-3643-0>.
- (23) Maeder, M. D.; Damjanovic, D.; Setter, N. Lead Free Piezoelectric Materials. *J. Electroceramics* **13** (1–3), 385–392. <https://doi.org/10.1007/s10832-004-5130-y>.
- (24) Kim, H.; Min Kim, S.; Son, H.; Kim, H.; Park, B.; Ku, J.; Inn Sohn, J.; Im, K.; Eun Jang, J.; Park, J.-J.; et al. Enhancement of Piezoelectricity via Electrostatic Effects on a Textile Platform. *Energy Environ. Sci.* **2012**, *5* (10), 8932–8936. <https://doi.org/10.1039/C2EE22744D>.
- (25) Matsubara, M.; Yamaguchi, T.; Sakamoto, W.; Kikuta, K.; Yogo, T.; Hirano, S. Processing and Piezoelectric Properties of Lead-Free (K,Na) (Nb,Ta) O₃

- Ceramics. *J. Am. Ceram. Soc.* **2005**, *88* (5), 1190–1196.
<https://doi.org/10.1111/j.1551-2916.2005.00229.x>.
- (26) Schilling, K.; Bradford, B.; Castelli, D.; Dufour, E.; Frank Nash, J.; Pape, W.; Schulte, S.; Tooley, I.; Bosch, J. van den; Schellauf, F. Human Safety Review of “Nano” Titanium Dioxide and Zinc Oxide. *Photochem. Photobiol. Sci.* **2010**, *9* (4), 495–509. <https://doi.org/10.1039/B9PP00180H>.
- (27) Monteiro-Riviere, N. A.; Wiench, K.; Landsiedel, R.; Schulte, S.; Inman, A. O.; Riviere, J. E. Safety Evaluation of Sunscreen Formulations Containing Titanium Dioxide and Zinc Oxide Nanoparticles in UVB Sunburned Skin: An In Vitro and In Vivo Study. *Toxicol. Sci.* **2011**, *123* (1), 264–280.
<https://doi.org/10.1093/toxsci/kfr148>.
- (28) Newman, M. D.; Stotland, M.; Ellis, J. I. The Safety of Nanosized Particles in Titanium Dioxide– and Zinc Oxide–Based Sunscreens. *J. Am. Acad. Dermatol.* **2009**, *61* (4), 685–692. <https://doi.org/10.1016/j.jaad.2009.02.051>.
- (29) Smijs, T. G.; Pavel, S. Titanium Dioxide and Zinc Oxide Nanoparticles in Sunscreens: Focus on Their Safety and Effectiveness. *Nanotechnol. Sci. Appl.* **2011**, *4*, 95–112. <https://doi.org/10.2147/NSA.S19419>.
- (30) Athauda, T. J.; Ozer, R. R. Nylon Fibers as Template for the Controlled Growth of Highly Oriented Single Crystalline ZnO Nanowires. *Cryst. Growth Des.* **2013**, *13* (6), 2680–2686. <https://doi.org/10.1021/cg400483d>.
- (31) Koka, A.; Zhou, Z.; Sodano, H. A. Vertically Aligned BaTiO₃ Nanowire Arrays for Energy Harvesting. *Energy Environ. Sci.* **2013**, *7* (1), 288–296.
<https://doi.org/10.1039/C3EE42540A>.
- (32) Magrez, A.; Vasco, E.; Seo, J. W.; Dieker, C.; Setter, N.; Forró, L. Growth of Single-Crystalline KNbO₃ Nanostructures. *J. Phys. Chem. B* **2006**, *110* (1), 58–61. <https://doi.org/10.1021/jp053800a>.
- (33) Jung, J. H.; Lee, M.; Hong, J.-I.; Ding, Y.; Chen, C.-Y.; Chou, L.-J.; Wang, Z. L. Lead-Free NaNbO₃ Nanowires for a High Output Piezoelectric Nanogenerator. *ACS Nano* **2011**, *5* (12), 10041–10046.
<https://doi.org/10.1021/nn2039033>.
- (34) Zhu, G.; Wang, A. C.; Liu, Y.; Zhou, Y.; Wang, Z. L. Functional Electrical Stimulation by Nanogenerator with 58 V Output Voltage. *Nano Lett.* **2012**, *12* (6), 3086–3090. <https://doi.org/10.1021/nl300972f>.
- (35) Saravanakumar, B.; Mohan, R.; Thiyagarajan, K.; Kim, S.-J. Fabrication of a ZnO Nanogenerator for Eco-Friendly Biomechanical Energy Harvesting. *RSC Adv.* **2013**, *3* (37), 16646–16656. <https://doi.org/10.1039/C3RA40447A>.
- (36) Lin, H.-I.; Wu, D.-S.; Shen, K.-C.; Horng, R.-H. Fabrication of an Ultra-Flexible ZnO Nanogenerator for Harvesting Energy from Respiration. *ECS J. Solid State Sci. Technol.* **2013**, *2* (9), P400–P404.
<https://doi.org/10.1149/2.001311jss>.
- (37) Liu, C.; Yu, A.; Peng, M.; Song, M.; Liu, W.; Zhang, Y.; Zhai, J. Improvement in the Piezoelectric Performance of a ZnO Nanogenerator by a Combination of Chemical Doping and Interfacial Modification. *J. Phys. Chem. C* **2016**, *120* (13), 6971–6977. <https://doi.org/10.1021/acs.jpcc.6b00069>.

- (38) Chang, C.; Tran, V. H.; Wang, J.; Fuh, Y.-K.; Lin, L. Direct-Write Piezoelectric Polymeric Nanogenerator with High Energy Conversion Efficiency. *Nano Lett.* **2010**, *10* (2), 726–731. <https://doi.org/10.1021/nl9040719>.
- (39) Kanik, M.; Aktas, O.; Sen, H. S.; Durgun, E.; Bayindir, M. Spontaneous High Piezoelectricity in Poly(Vinylidene Fluoride) Nanoribbons Produced by Iterative Thermal Size Reduction Technique. *ACS Nano* **2014**, *8* (9), 9311–9323. <https://doi.org/10.1021/nn503269b>.
- (40) Cheng, B.; T. Samulski, E. Hydrothermal Synthesis of One-Dimensional ZnO Nanostructures with Different Aspect Ratios. *Chem. Commun.* **2004**, *0* (8), 986–987. <https://doi.org/10.1039/B316435G>.
- (41) ImageJ <https://imagej.nih.gov/ij/> (accessed May 30, 2018).
- (42) Lord, M. Foot Pressure Measurement: A Review of Methodology. *J. Biomed. Eng.* **1981**, *3* (2), 91–99. [https://doi.org/10.1016/0141-5425\(81\)90001-7](https://doi.org/10.1016/0141-5425(81)90001-7).
- (43) Urry, S. Plantar Pressure-Measurement Sensors. *Meas. Sci. Technol.* **1999**, *10* (1), R16. <https://doi.org/10.1088/0957-0233/10/1/017>.
- (44) Duckworth, T.; Betts, R. P.; Franks, C. I.; Burke, J. The Measurement of Pressures under the Foot. *Foot Ankle* **1982**, *3* (3), 130–141. <https://doi.org/10.1177/107110078200300303>.
- (45) Lanceros-Méndez, S.; Mano, J. F.; Costa, A. M.; Schmidt, V. H. FTIR AND DSC STUDIES OF MECHANICALLY DEFORMED β -PVDF FILMS. *J. Macromol. Sci. Part B* **2001**, *40* (3–4), 517–527. <https://doi.org/10.1081/MB-100106174>.
- (46) Bormashenko, Y.; Pogreb, R.; Stanevsky, O.; Bormashenko, E. Vibrational Spectrum of PVDF and Its Interpretation. *Polym. Test.* **2004**, *23* (7), 791–796. <https://doi.org/10.1016/j.polymertesting.2004.04.001>.
- (47) Salimi, A.; Yousefi, A. A. Analysis Method: FTIR Studies of β -Phase Crystal Formation in Stretched PVDF Films. *Polym. Test.* **2003**, *22* (6), 699–704. [https://doi.org/10.1016/S0142-9418\(03\)00003-5](https://doi.org/10.1016/S0142-9418(03)00003-5).
- (48) Martins, P.; Lopes, A. C.; Lanceros-Mendez, S. Electroactive Phases of Poly(Vinylidene Fluoride): Determination, Processing and Applications. *Prog. Polym. Sci.* **2014**, *39* (4), 683–706. <https://doi.org/10.1016/j.progpolymsci.2013.07.006>.
- (49) Gregorio, J., Rinaldo; Cestari, M. Effect of Crystallization Temperature on the Crystalline Phase Content and Morphology of Poly(Vinylidene Fluoride). *J. Polym. Sci. Part B Polym. Phys.* **1994**, *32* (5), 859–870. <https://doi.org/10.1002/polb.1994.090320509>.
- (50) Liu, B.; Zeng, H. C. Hydrothermal Synthesis of ZnO Nanorods in the Diameter Regime of 50 Nm. *J. Am. Chem. Soc.* **2003**, *125* (15), 4430–4431. <https://doi.org/10.1021/ja0299452>.
- (51) Geng, C.; Jiang, Y.; Yao, Y.; Meng, X.; Zapien, J. A.; Lee, C. S.; Lifshitz, Y.; Lee, S. T. Well-Aligned ZnO Nanowire Arrays Fabricated on Silicon Substrates. *Adv. Funct. Mater.* **2004**, *14* (6), 589–594. <https://doi.org/10.1002/adfm.200305074>.
- (52) Chen, C.; Kelder, E. M.; Schoonman, J. Functional Ceramic Films with Reticular Structures Prepared by Electrostatic Spray Deposition Technique. *J.*

- Electrochem. Soc.* **1997**, *144* (11), L289–L291.
<https://doi.org/10.1149/1.1838071>.
- (53) Hjiri, M.; El Mir, L.; Leonardi, S. G.; Pistone, A.; Mavilia, L.; Neri, G. Al-Doped ZnO for Highly Sensitive CO Gas Sensors. *Sens. Actuators B Chem.* **2014**, *196*, 413–420. <https://doi.org/10.1016/j.snb.2014.01.068>.
- (54) Athauda, T. J.; Neff, J. G.; Sutherlin, L.; Butt, U.; Ozer, R. R. Systematic Study of the Structure–Property Relationships of Branched Hierarchical TiO₂/ZnO Nanostructures. *ACS Appl. Mater. Interfaces* **2012**, *4* (12), 6917–6926. <https://doi.org/10.1021/am302061z>.
- (55) Xu, S.; Wang, Z. L. One-Dimensional ZnO Nanostructures: Solution Growth and Functional Properties. *Nano Res.* **2011**, *4* (11), 1013–1098. <https://doi.org/10.1007/s12274-011-0160-7>.
- (56) Baruah, S.; Thanachayanont, C.; Dutta, J. Growth of ZnO Nanowires on Nonwoven Polyethylene Fibers. *Sci. Technol. Adv. Mater.* **2008**, *9* (2), 025009. <https://doi.org/10.1088/1468-6996/9/2/025009>.
- (57) Kolbeck, A. G. Aging of Piezoelectricity in Poly(Vinylidene Fluoride). *J. Polym. Sci. Polym. Phys. Ed.* **1982**, *20* (11), 1987–2001. <https://doi.org/10.1002/pol.1982.180201102>.
- (58) Sugunan, A.; Warad, H. C.; Boman, M.; Dutta, J. Zinc Oxide Nanowires in Chemical Bath on Seeded Substrates: Role of Hexamine. *J. Sol-Gel Sci. Technol.* **2006**, *39* (1), 49–56. <https://doi.org/10.1007/s10971-006-6969-y>.
- (59) Kim, M.; Wu, Y. S.; Kan, E. C.; Fan, J. Breathable and Flexible Piezoelectric ZnO@PVDF Fibrous Nanogenerator for Wearable Applications. *Polymers* **2018**, *10* (7), 745. <https://doi.org/10.3390/polym10070745>.
- (60) Soin, N.; H. Shah, T.; C. Anand, S.; Geng, J.; Pornwannachai, W.; Mandal, P.; Reid, D.; Sharma, S.; L. Hadimani, R.; Vatansever Bayramol, D.; et al. Novel “3-D Spacer” All Fibre Piezoelectric Textiles for Energy Harvesting Applications. *Energy Environ. Sci.* **2014**, *7* (5), 1670–1679. <https://doi.org/10.1039/C3EE43987A>.
- (61) Fang, J.; Wang, X.; Lin, T. Electrical Power Generator from Randomly Oriented Electrospun Poly(Vinylidene Fluoride) Nanofibre Membranes. *J. Mater. Chem.* **2011**, *21* (30), 11088–11091. <https://doi.org/10.1039/C1JM11445J>.
- (62) Liu, Z. H.; Pan, C. T.; Lin, L. W.; Huang, J. C.; Ou, Z. Y. Direct-Write PVDF Nonwoven Fiber Fabric Energy Harvesters via the Hollow Cylindrical near-Field Electrospinning Process. *Smart Mater. Struct.* **2014**, *23* (2), 025003. <https://doi.org/10.1088/0964-1726/23/2/025003>.
- (63) He, F.; Sarkar, M.; Lau, S.; Fan, J.; Chan, L. H. Preparation and Characterization of Porous Poly(Vinylidene Fluoride-Trifluoroethylene) Copolymer Membranes via Electrospinning and Further Hot Pressing. *Polym. Test.* **2011**, *30* (4), 436–441. <https://doi.org/10.1016/j.polymertesting.2011.03.005>.
- (64) Wu, Y.-K.; Wang, L.; Fan, J.; Shou, W.; Zhou, B.-M.; Liu, Y. Multi-Jet Electrospinning with Auxiliary Electrode: The Influence of Solution Properties. *Polymers* **2018**, *10* (6), 572. <https://doi.org/10.3390/polym10060572>.

- (65) Athauda, T. J.; Butt, U.; Ozer, R. R. One-Dimensional Hierarchical Composite Materials Based on ZnO Nanowires and Electrospun Blend Nanofibers. *RSC Adv.* **2013**, *3* (44), 21431–21438. <https://doi.org/10.1039/C3RA43672A>.
- (66) Wang, G.; Deng, Y.; Xiang, Y.; Guo, L. Fabrication of Radial ZnO Nanowire Clusters and Radial ZnO/PVDF Composites with Enhanced Dielectric Properties. *Adv. Funct. Mater.* **2008**, *18* (17), 2584–2592. <https://doi.org/10.1002/adfm.200800109>.
- (67) Polsongkram, D.; Chamninok, P.; Pukird, S.; Chow, L.; Lupan, O.; Chai, G.; Khallaf, H.; Park, S.; Schulte, A. Effect of Synthesis Conditions on the Growth of ZnO Nanorods via Hydrothermal Method. *Phys. B Condens. Matter* **2008**, *403* (19–20), 3713–3717. <https://doi.org/10.1016/j.physb.2008.06.020>.
- (68) Shin, Y. M.; Hohman, M. M.; Brenner, M. P.; Rutledge, G. C. Electrospinning: A Whipping Fluid Jet Generates Submicron Polymer Fibers. *Appl. Phys. Lett.* **2001**, *78* (8), 1149–1151. <https://doi.org/10.1063/1.1345798>.
- (69) Baji, A.; Mai, Y.-W.; Wong, S.-C.; Abtahi, M.; Chen, P. Electrospinning of Polymer Nanofibers: Effects on Oriented Morphology, Structures and Tensile Properties. *Compos. Sci. Technol.* **2010**, *70* (5), 703–718. <https://doi.org/10.1016/j.compscitech.2010.01.010>.
- (70) Hohman, M. M.; Shin, M.; Rutledge, G.; Brenner, M. P. Electrospinning and Electrically Forced Jets. I. Stability Theory. *Phys. Fluids* **2001**, *13* (8), 2201–2220. <https://doi.org/10.1063/1.1383791>.
- (71) Mandal, D.; Yoon, S.; Kim, K. J. Origin of Piezoelectricity in an Electrospun Poly(Vinylidene Fluoride-Trifluoroethylene) Nanofiber Web-Based Nanogenerator and Nano-Pressure Sensor. *Macromol. Rapid Commun.* **2011**, *32* (11), 831–837. <https://doi.org/10.1002/marc.201100040>.
- (72) Tsai, C.-C.; Mikes, P.; Andruk, T.; White, E.; Monaenkova, D.; Burtovyy, O.; Burtovyy, R.; Rubin, B.; Lukas, D.; Luzinov, I.; et al. Nanoporous Artificial Proboscis for Probing Minute Amount of Liquids. *Nanoscale* **2011**, *3* (11), 4685–4695. <https://doi.org/10.1039/C1NR10773A>.
- (73) Huang, J.; Qian, X. Comparison of Test Methods for Measuring Water Vapor Permeability of Fabrics. *Text. Res. J.* **2008**, *78* (4), 342–352. <https://doi.org/10.1177/0040517508090494>.
- (74) Indushekar, R.; Awasthi, P.; Gupta, R. K.; Kotresh, T. M. Studies on Test Methods Used to Measure Water Vapor Transmission of Fabrics by DSC and Conventional Dish Techniques. *J. Ind. Text.* **2005**, *34* (4), 223–242. <https://doi.org/10.1177/1528083705051454>.
- (75) Bagherzadeh, R.; Latifi, M.; Najar, S. S.; Tehran, M. A.; Gorji, M.; Kong, L. Transport Properties of Multi-Layer Fabric Based on Electrospun Nanofiber Mats as a Breathable Barrier Textile Material. *Text. Res. J.* **2012**, *82* (1), 70–76. <https://doi.org/10.1177/0040517511420766>.
- (76) Shou, D.; Ye, L.; Fan, J. Gas Transport Properties of Electrospun Polymer Nanofibers. *Polymer* **2014**, *55* (14), 3149–3155. <https://doi.org/10.1016/j.polymer.2014.05.016>.

- (77) Shou, D.; Fan, J.; Mei, M.; Ding, F. An Analytical Model for Gas Diffusion Through Nanoscale and Microscale Fibrous Media. *Microfluid. Nanofluidics* **2014**, *16* (1–2), 381–389. <https://doi.org/10.1007/s10404-013-1215-8>.
- (78) Jedda, H.; Ghith, A.; Sakli, F. Prediction of Fabric Drape Using the FAST System. *J. Text. Inst.* **2007**, *98* (3), 219–225. <https://doi.org/10.1080/00405000701463920>.
- (79) Wang, X.; Sun, F.; Yin, G.; Wang, Y.; Liu, B.; Dong, M. Tactile-Sensing Based on Flexible PVDF Nanofibers via Electrospinning: A Review. *Sensors* **2018**, *18* (2), 330. <https://doi.org/10.3390/s18020330>.
- (80) Soin, N.; Zhao, P.; Prashanthi, K.; Chen, J.; Ding, P.; Zhou, E.; Shah, T.; Ray, S. C.; Tsonos, C.; Thundat, T.; et al. High Performance Triboelectric Nanogenerators Based on Phase-Inversion Piezoelectric Membranes of Poly(Vinylidene Fluoride)-Zinc Stannate (PVDF-ZnSnO₃) and Polyamide-6 (PA6). *Nano Energy* **2016**, *30*, 470–480. <https://doi.org/10.1016/j.nanoen.2016.10.040>.
- (81) Wang, X.; Yang, B.; Liu, J.; Zhu, Y.; Yang, C.; He, Q. A Flexible Triboelectric-Piezoelectric Hybrid Nanogenerator Based on P(VDF-TrFE) Nanofibers and PDMS/MWCNT for Wearable Devices. *Sci. Rep.* **2016**, *6*, 36409. <https://doi.org/10.1038/srep36409>.
- (82) Wang, Y.; Yang, Y.; Wang, Z. L. Triboelectric Nanogenerators as Flexible Power Sources. *Npj Flex. Electron.* **2017**, *1* (1). <https://doi.org/10.1038/s41528-017-0007-8>.
- (83) Lee, J. P.; Lee, J. W.; Baik, J. M. The Progress of PVDF as a Functional Material for Triboelectric Nanogenerators and Self-Powered Sensors. *Micromachines* **2018**, *9* (10), 532. <https://doi.org/10.3390/mi9100532>.